Low Complex Methods for Robust Channel Estimation in Doubly Dispersive Environments

Abdul Karim Gizzini, Marwa Chafii

Date of publication xxxx 00, 0000, date of current version xxxx 00, 0000.

Digital Object Identifier 10.1109/ACCESS.2017.DOI

Low Complex Methods for Robust Channel Estimation in Doubly Dispersive Environments

ABDUL KARIM GIZZINI[1], MARWA CHAFII[2,3]
[1]ETIS, UMR8051, CY Cergy Paris Université, ENSEA, CNRS, France (e-mail: abdulkarim.gizzini@ensea.fr)
[2]Engineering Division, New York University (NYU) Abu Dhabi, 129188, UAE
[3]NYU WIRELESS, NYU Tandon School of Engineering, Brooklyn, 11201, NY (e-mail: marwa.chafii@nyu.edu).

Corresponding author: Abdul Karim Gizzini (e-mail: abdulkarim.gizzini@ensea.fr).

ABSTRACT

Wireless communications play a significant role in facilitating several mobile applications like unmanned aerial vehicles, high-speed railway, and vehicular communications. Particularly, the concept of connected vehicles brings a new level of connectivity to vehicles. Along with novel on-board computing and sensing technologies, vehicular networks serve as a key enabler of intelligent transportation systems and smart cities. However, in such environments, the propagation medium between the network nodes is highly time-varying leading to considerable reliability challenges. Ensuring communication reliability by the means of accurate channel estimation in such environments is very important. Initially, vehicular communications standards apply the basic least square (LS) estimation that is not enough for the dynamic vehicular environment. Moreover, the frame structure has low pilot density, making channel tracking a difficult task to achieve, especially in high mobility scenarios. Conventional estimators either employ data subcarriers besides pilots in the estimation process, or the estimated channel and noise statistics. Therefore they suffer from significant performance degradation due to high error probability resulting from hard symbol demapping and the sensitivity against the change in the employed channel statistics. The motivation behind this paper is to overcome this challenge by proposing a low complex and robust channel estimation scheme based on truncated discrete Fourier transform (T-DFT) that updates the channel estimates using DFT interpolation without the need for data subcarriers decisions and the estimated channel statistics. Moreover, further performance improvement can be achieved by considering temporal averaging on top of T-DFT estimation. Analytical and simulation results carried out using different vehicular channel models reveal the performance superiority of the proposed schemes compared to conventional estimators while recording a significant decrease in computational complexity and execution time.

INDEX TERMS Channel estimation, vehicular communications, DFT interpolation.

I. INTRODUCTION

VEHICULAR communications [1] have been introduced to facilitate several future smart city applications such as safety, infotainment, roadway information dissemination, and autonomous driving. By staying connected, vehicles can more efficiently communicate with each other, therefore mitigating traffic accidents that are considered one of the leading causes of death all over the world [2]. Two vehicular communications standards have been proposed: (*i*) WiFi-based where IEEE 802.11p initially proposed to manage vehicular communications [3], [4]. (*ii*) Cellular-based where LTE and 5G networks are employed in vehicular communications [5]. In this work we focus on the IEEE 802.11p WiFi-based standard that have been proposed to meet vehicular communications needs, especially communication reliability that represents the most important feature in managing real-time applications. However, we note that the proposed work can be generalized to any other standard that manages wireless communications in doubly-dispersive channels.

Both vehicle-to-vehicle (V2V) and vehicle-to-infrastructure (V2I) communications suffer from a harsh signal propagation environment mainly due to the following two reasons: (*i*) One or both communications nodes i.e. the transmitter and the receiver are in motion. As a result, the vehicular channel

variation raises as the vehicle velocity increases, leading to a short channel coherence time. (*ii*) There are fixed and mobile scatterers that introduce significant channel multi-path components. Therefore, the vehicular channel becomes doubly selective, i.e. in time and frequency and its estimation is then challenging.

IEEE 802.11p standard allocates two full preamble symbols at the beginning of each frame that are used for channel estimation at the receiver using the basic least square (LS) estimator [6]. Moreover, the channel is estimated once for each frame, and the estimated channel is used to equalize the whole frame. Due to the time-varying nature of the vehicular channel, the basic estimated channel can quickly become outdated, resulting in overall poor system performance. Therefore, to track the channel, four pilots are multiplexed with the data subcarriers in each transmitted symbol.

Conventional channel estimators that have been proposed for the IEEE 802.11p standard assume that the allocated pilot subcarriers are not sufficient for accurately tracking the vehicular channel, since they are not spaced closely enough to capture the variation of the channel in the frequency domain. Therefore, IEEE 802.11p conventional estimators are mainly based on the demapped data subcarriers, besides pilot subcarriers to update the channel estimate for each received symbol. This procedure is referred to as data-pilot aided (DPA) channel estimation. In order to improve the basic channel estimation performance, the spectral temporal averaging (STA) estimator [7] applies averaging in both the time and the frequency domains as post-processing operations on top of DPA estimation. STA estimator outperforms other conventional estimators in low signal-to-noise ratio (SNR) region, while it suffers from significant performance degradation in high SNR region especially in high mobility vehicular scenarios. Constructed data pilots (CDP) estimator [8] assumes a high correlation between each two successive received symbols, thus the final estimated channels are updated over the received frame according to this assumption. CDP estimator outperforms STA estimator especially in high SNR region but still cannot perform well in high mobility scenarios when high modulation orders are employed. Improved CDP (iCDP) [9] estimator combines both STA and CDP estimators, thus the overall performance in the whole SNR region is improved. In [10], the authors proposed the time domain reliable test frequency domain interpolation (TRFI) estimator that utilizes frequency domain interpolation in order to also improve the CDP estimator. Inspired by the conventional TRFI estimator, the authors in [11] proposed an enhanced TRFI E-TRFI estimator, where the employed interpolation utilizes all the subcarriers within the received symbol to improve the interpolation accuracy. After that, a noise attenuation step is employed leading to improved overall performance. E-TRFI outperforms STA, CDP, and TRFI estimators especially in the high SNR region, but similarly to the other conventional estimators, it suffers from considerable performance degradation in high mobility vehicular scenarios. Another conventional approach is to employ the linear minimum mean square error (LMMSE) estimator [12] where the estimated channel and noise statistics are utilized in the channel estimation. The LMMSE estimator does not depend on the DPA estimation, therefore, it outperforms the conventional DPA-based estimators. However, LMMSE suffers from significant performance degradation when there is a mismatch between the estimated and real channel and noise statistics represented by the channel correlation matrices and the noise power. Therefore, making it impractical in such scenarios.

The performance degradation of the conventional estimators is mainly related to two reasons: (*i*) Conventional estimators are based initially on the basic LS channel estimation applied at the received preamble symbols. This basic estimation utilizes only the predefined preamble sequence in the frequency domain, without taking into consideration the LS estimation at the channel delay taps. Thus, it ignores the relationship between the channel taps, and the presence of noise in the estimation process. Therefore, basic LS estimation is noisy and unreliable to be considered as a starting point of the conventional estimators. (*ii*) Conventional estimators employ the DPA estimation, which is based on demapping the received data subcarriers and using them as pilots. This mechanism is also unreliable since the demapping error is enlarged from one symbol to another, hence leading to an additional error in the estimation process.

Therefore, in order to overcome the drawbacks of the conventional estimators, in this paper, we propose an estimation method that depends mainly on employing the tracking pilots without considering the basic LS estimation at the preamble, the DPA estimation, and the estimated channel and noise statistics. As a result, the data subcarriers demapping step is not required and the demapping error is completely eliminated, resulting in better estimation accuracy.

Based on the above context, in this paper, we propose a robust, low complex channel estimation scheme for IEEE 802.11p standard that is based on truncated discrete Fourier transform (T-DFT) interpolation, where the classical DFT interpolation is adapted to the IEEE 802.11p standard structure by employing the pilot subcarriers within each symbol to estimate the dominant vehicular channel taps. Moreover, we show that updating the estimated channels for the received symbols using time-averaged T-DFT leads to considerable noise alleviation throughout the frame, resulting in reducing the bit error rate (BER) and normalized mean-squared error (NMSE) performance. The contributions in this paper can be listed as follows

- A low complex T-DFT channel estimation scheme is proposed. It adapts the DFT-based channel estimation to the IEEE 802.11p standard by estimating only the channel impulse response of dominant taps using the predefined pilots. It is worth mentioning, that the proposed estimator can be easily adapted to other standards that have different parameters i.e. in terms of number of subcarriers and number of allocated pilots.

TABLE 1: IEEE 802.11p modulation orders and data rates.

Modulation orders	BPSK		QPSK		16QAM		64QAM	
Coding rate	$\frac{1}{2}$	$\frac{3}{4}$	$\frac{1}{2}$	$\frac{3}{4}$	$\frac{1}{2}$	$\frac{3}{4}$	$\frac{2}{3}$	$\frac{3}{4}$
Data rate (Mbps)	3	4.5	6	9	12	18	24	27
Data bits per OFDM symbol	24	36	48	72	96	144	192	216

- The temporal averaging T-DFT (TA-TDFT) scheme is proposed, which applies an appropriate temporal averaging to T-DFT in order to enhance the estimation performance which results in an improved BER and NMSE performance in different vehicular channels conditions.
- Analytical derivations of the NMSE expressions of T-DFT and TA-TDFT are developed and demonstrate how the noise power is degraded throughout the received frame.
- The proposed T-DFT and TA-TDFT estimators employ only the tracking pilots without the DPA estimation step, thus, the enlarged DPA de-mapping error is totally eliminated. Moreover, they do not depend on the pre-estimated channel correlation matrices and SNR estimation. Therefore, achieving a considerable robustness superiority compared to conventional LMMSE estimator in case of mismatch between the pre-estimated and the real channel correlation matrices and SNR estimation.
- A detailed computational complexity and execution time analysis is provided for the studied channel estimators, where we show that the proposed T-DFT-based schemes outperform conventional estimators with less computational complexity and execution time.

The remainder of this paper is organized as follows: in Section II, the IEEE 802.11p standard and the system model are described. Section III provides a detailed description of the conventional channel estimations schemes. The proposed T-DFT and TA-TDFT schemes, as well as their analytical NMSE derivations, are described in Section IV. In Section V, simulation results are presented for different vehicular channel models conditions employing different modulation orders, where the performance of the proposed schemes is evaluated in terms of BER and NMSE. Detailed computational complexity and execution time analysis are provided in Section VI. Finally, the paper is concluded in Section VII.

Notations: Throughout the paper, vectors are defined with lowercase bold symbols $\boldsymbol{x}$ whose k-th element is $\boldsymbol{x}[k]$. Time and frequency domain vectors are represented by $\boldsymbol{x}$ and $\tilde{\boldsymbol{x}}$ respectively. Matrices are written as uppercase bold symbols $\boldsymbol{X}$. $\mathrm{E}[.]$ is the expectation operator. The trace of a square matrix $\boldsymbol{X}$ is $\mathrm{trace}\{\boldsymbol{X}\}$. The notation $\odot$ and $\oslash$ denote the element-wise multiplication and division operations, respectively. Finally. the pseudo inverse and conjugate matrices of $\boldsymbol{X}$ are denoted by $\boldsymbol{X}^{\dagger}$ and $\boldsymbol{X}^{\mathrm{H}}$ respectively.

II. IEEE 802.11P SYSTEM MODEL

IEEE 802.11p is an approved upgrade of the IEEE 802.11a standard that adds wireless access in vehicular environments. This upgrade includes data exchange between high-speed vehicles (V2V) and between the vehicles and the roadside infrastructure (V2I) in the licensed intelligent transportation systems band [13]. IEEE 802.11p supports sending data at different data rates employing different modulation orders, as described in Table 1. Moreover, it employs orthogonal frequency-division multiplexing (OFDM) transmission scheme with $K = 64$ total subcarriers. $K_{\mathrm{on}} = 52$ active subcarriers are used, and they are divided into $K_{\mathrm{d}} = 48$ data subcarriers and $K_{\mathrm{p}} = 4$ pilot subcarriers. The remaining $K_{\mathrm{n}} = 12$ subcarriers are used as a guard band. Compared to the IEEE 802.11a standard, the channel bandwidth is halved, resulting in a 10 MHz bandwidth instead of 20 MHz in 802.11a. Also, the carrier spacing is reduced by half. Moreover, all OFDM timing parameters used in the regular 802.11a are doubled. This enhances the system reliability required by vehicular communications applications since a larger guard interval reduces the inter-symbol interference caused by multi-path propagation. Table 2 shows the IEEE 802.11p physical layer specifications. A detailed discussion of the IEEE 802.p and its features are presented in [6].

A. IEEE 802.11P FRAME STRUCTURE AND SIGNAL MODEL

An IEEE 802.11p frame consists mainly of three parts: (*i*) preamble, (*ii*) signal field, and (*iii*) OFDM data symbols. The preamble includes ten short training symbols (STS) t_1 to t_{10}, each of duration 1.6 μs. The STS are used at the receiver for signal detection, diversity selection, coarse frequency offset estimation, and timing synchronization. The following two 6.4 μs long training symbols (LTS) are prepended with a cyclic prefix (CP) of duration 3.2 μs and used for channel estimation at the receiver. After that, the signal field is used to specify the rate and length information that is required for decoding the received OFDM data symbols. It consists of one CP-OFDM symbol that carries 24 bits divided into four fields as follows

- **Rate**: the first 4 bits convey information about the employed modulation and coding rate.
- **Length**: 12 bits integer (6 to 17) that indicate the number of data octets requested in the transmission.
- **Reserved**: bits 5 and 18 that are reserved for future use.
- **Tail**: the last 6 bits that are set to zeros and used to synchronize the descrambler at the receiver, and to return the convolutional encoder to the zero state.

Finally, the OFDM data symbols that carry the actually transmitted data bits are inserted. Figure 1 illustrates the IEEE 802.11p frame structure in the time domain. In this paper, we assume perfect synchronization at the receiver, and we ignore the signal field for simplicity. Therefore, we focus on a frame that consists of two LTS at the beginning followed by I OFDM data symbols. The i-th transmitted frequency-

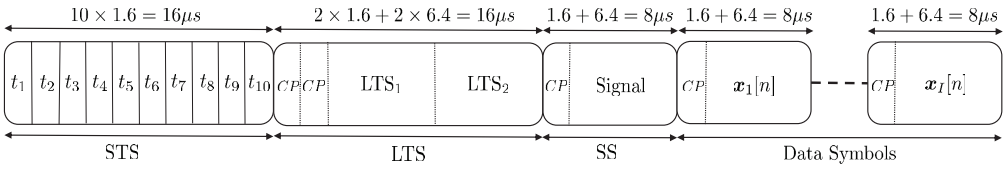

FIGURE 1: IEEE 802.11p transmitted frame structure in the time domain.

domain OFDM symbol $\tilde{\boldsymbol{x}}_i[k]$, is partitioned as

$$\tilde{\boldsymbol{x}}_i[k] = \begin{cases} \tilde{\boldsymbol{x}}_{\mathrm{d}_i}[k], & k \in \mathcal{K}_{\mathrm{d}}. \\ \tilde{\boldsymbol{x}}_{\mathrm{p}_i}[k], & k \in \mathcal{K}_{\mathrm{p}}. \\ 0, & k \in \mathcal{K}_{\mathrm{n}}, \end{cases} \tag{1}$$

where $0 \leq k \leq K-1$. $\tilde{\boldsymbol{x}}_{\mathrm{d}_i}[k]$ and $\tilde{\boldsymbol{x}}_{\mathrm{p}_i}[k]$ denote the modulated data symbols and the predefined pilot symbols allocated at a set of subcarriers denoted $\mathcal{K}_{\mathrm{d}}$ and $\mathcal{K}_{\mathrm{p}}$, respectively. The other guard band subcarriers are allocated at the set of subcarriers $\mathcal{K}_{\mathrm{n}}$. $\boldsymbol{x}_i[k]$ is converted to the time domain by applying the inverse discrete Fourier transform, such that

$$\boldsymbol{x}_i[n] = \frac{1}{\sqrt{K}} \sum_{k=0}^{K-1} \tilde{\boldsymbol{x}}_i[k] e^{j2\pi \frac{nk}{K}}. \tag{2}$$

B. RECEIVED SIGNAL AND CHANNEL MODEL

After passing through the doubly-selective vehicular channel, the received OFDM symbol $\boldsymbol{y}_i[n]$ can be expressed as

$$\begin{aligned} \boldsymbol{y}_i[n] &= \sum_{l=0}^{L-1} \boldsymbol{h}_i[l,n] \boldsymbol{x}_i[n-l] + \boldsymbol{v}_i[n] \\ &= \frac{1}{\sqrt{K}} \sum_{k=0}^{K-1} \tilde{\boldsymbol{h}}_i[k,n] \tilde{\boldsymbol{x}}_i[k] e^{j2\pi \frac{nk}{K}} + \boldsymbol{v}_i[n], \end{aligned} \tag{3}$$

where $\boldsymbol{h}_i[l,n]$ denotes the delay-time response of the discrete linear time-variant (LTV) channel of L taps at the i-th OFDM symbol, whereas $\tilde{\boldsymbol{h}}_i[k,n] = \sum_{l=0}^{L-1} \boldsymbol{h}_i[l,n] e^{-j2\pi \frac{lk}{K}}$ is the frequency-time response. Moreover, $\boldsymbol{v}_i$ denotes the additive white Gaussian noise (AWGN) of variance σ^2. The i-th received frequency-domain OFDM symbol is obtained from (3) by means of discrete Fourier transform (DFT), and thus

$$\tilde{\boldsymbol{y}}_i[k] = \frac{1}{K} \sum_{q=0}^{K-1} \tilde{\boldsymbol{x}}_i[q] \sum_{n=0}^{K-1} \tilde{\boldsymbol{h}}_i[q,n] e^{-j2\pi \frac{n(k-q)}{K}} + \tilde{\boldsymbol{v}}_i[k]. \tag{4}$$

Note that $\tilde{\boldsymbol{h}}_i[q,n]$ is time-variant at the scale of the OFDM symbol duration and within the symbol itself. Accordingly

$$\tilde{\boldsymbol{h}}_i[q,n] = \sum_{l=0}^{L-1} e^{-j2\pi \frac{lq}{K}} \int_{\nu=-\nu_d}^{\nu=\nu_d} \bar{h}(l,\nu) e^{j2\pi\nu n_i} e^{j2\pi\nu n} d\nu, \tag{5}$$

where $\bar{h}(l,\nu) = \sum_n h[l,n] e^{-j2\pi n\nu}$ is the channel delay-Doppler response, ν denotes the normalized Doppler frequency, $n_i = i(K + K_{\mathrm{cp}}) + K_{\mathrm{cp}}$. And $\nu_d = \frac{f_d}{F_s}$ is the maximum Doppler frequency. Let

$$\begin{aligned} \bar{\boldsymbol{h}}_i[l,v] &= \frac{1}{K} \sum_{q=0}^{K-1} \sum_{n=0}^{K-1} \tilde{\boldsymbol{h}}_i[q,n] e^{-j2\pi \frac{nv}{K}} e^{j2\pi \frac{ql}{K}} \\ &= \int_{\nu=-\nu_d}^{\nu=\nu_d} \bar{h}(l,\nu) e^{j2\pi\nu n_i} \sum_{n=0}^{K-1} e^{-j2\pi(\nu - \frac{v}{K})n} d\nu, \end{aligned} \tag{6}$$

be the discrete delay-Doppler response at the i-th OFDM symbol. For simplicity, we assume $\bar{h}(l,\nu)$ to be uncorrelated in both domains, such that $\mathrm{E}\left[\bar{h}(l,\nu)\bar{h}^*(l',\nu')\right] = S_h(l,\nu)\delta[l-l']\delta(\nu-\nu')$, where $S_h(l,\nu)$ is the delay-Doppler spectrum [14], then using (6), we have

$$\begin{aligned} &\mathrm{E}\left[\bar{\boldsymbol{h}}_i[l,v]\bar{\boldsymbol{h}}_i^*[l,v']\right] = \\ &\int_{\nu=-\nu_d}^{\nu=\nu_d} S_h(l,\nu) \sum_{n=0}^{K-1} \sum_{n'=0}^{K-1} e^{-j2\pi\nu(n-n')} e^{-j2\pi \frac{n'v'-nv}{K}} d\nu. \end{aligned} \tag{7}$$

This correlation is independent of the index i, and it can be approximated as

$$\mathrm{E}\left[\bar{\boldsymbol{h}}_i[l,v]\bar{\boldsymbol{h}}_i^*[l,v']\right] \approx K^2 \rho[l,v]\delta[v-v'],\ \rho[l,v] = S_h(l, \frac{v}{N}). \tag{8}$$

The time selectivity of the channel depends on mobility. In very low mobility, where $f_{\mathrm{d}} \approx 0$, $\tilde{\boldsymbol{h}}_i[q,n] = \tilde{\boldsymbol{h}}[q]$ is constant during the whole frame. For moderate to high mobility, the channel variation within the duration of one OFDM symbol is negligible, and therefore, $\tilde{\boldsymbol{h}}_i[q,n] = \tilde{\boldsymbol{h}}_i[q]$. At very high mobility, the channel becomes variant within a single OFDM symbol. In this case, $\tilde{\boldsymbol{h}}_i[q,n] = \tilde{\boldsymbol{h}}_i[q] + \tilde{\boldsymbol{\epsilon}}_i[q,n]$, where

$$\tilde{\boldsymbol{h}}_i[q] = \frac{1}{K} \sum_{n=0}^{K-1} \tilde{\boldsymbol{h}}_i[q,n], \text{ and } \tilde{\boldsymbol{\epsilon}}_i[q,n] = \tilde{\boldsymbol{h}}_i[q,n] - \tilde{\boldsymbol{h}}_i[q]. \tag{9}$$

Replacing this in (4), we get the full equation of the signal model represented by

$$\boxed{\tilde{\boldsymbol{y}}_i[k] = \tilde{\boldsymbol{h}}_i[k]\tilde{\boldsymbol{x}}_i[k] + \tilde{\boldsymbol{e}}_{i,\mathrm{d}}[k] + \tilde{\boldsymbol{v}}_i[k],\ k \in \mathcal{K}_{\mathrm{on}}.} \tag{10}$$

The term $\tilde{\boldsymbol{e}}_{i,\mathrm{d}}[k]$ represents the Doppler interference given by

$$\begin{aligned} \tilde{\boldsymbol{e}}_{i,\mathrm{d}}[k] &= \frac{1}{K} \sum_{\substack{q=0 \\ q \neq k}}^{K-1} \sum_{n=0}^{K-1} \tilde{\boldsymbol{h}}_i[q,n] e^{-j2\pi \frac{n(k-q)}{K}} \tilde{\boldsymbol{x}}_i[q] \\ &= \frac{1}{K} \sum_{\substack{q \in \mathcal{K}_{\mathrm{on}} \\ q \neq k}} \sum_{l=0}^{L-1} \bar{\boldsymbol{h}}_i[l, k-q] e^{-j2\pi \frac{lq}{K}} \tilde{\boldsymbol{x}}_i[q]. \end{aligned} \tag{11}$$

TABLE 2: IEEE 802.11p physical layer specifications.

Parameter	IEEE 802.11p
Bandwidth	10 MHz
Carrier frequency	5.9 GHz
CP duration	1.6 μs
Symbol duration	8 μs
STS duration	1.6 μs
LTS duration	6.4 μs
Overall STS duration	16 μs
Overall LTS duration	16 μs
Total subcarriers	64
Pilot subcarriers	4
Data subcarriers	48
Null subcarriers	12
$\mathcal{K}_{\rm p}$	$\{\pm 7, \pm 21\}$
$\mathcal{K}_{\rm n}$	$\{0, \pm 27, \pm 28, \pm 29, \pm 30, \pm 31, -32\}$
$\mathcal{K}_{\rm d}$	$\mathcal{K}_{\rm on} \setminus \mathcal{K}_{\rm p} \cup \mathcal{K}_{\rm n}$
Subcarrier spacing	156.25 KHz

The Doppler interference destroys the orthogonality of the subcarriers within the received OFDM symbol, resulting in a significant degradation in the overall system performance [15]. Assuming the subcarriers are uncorrelated with power E_q, i.e. $\mathrm{E}\left[\tilde{\boldsymbol{x}}_i[q]\tilde{\boldsymbol{x}}_i^*[q']\right] = E_q\delta[q-q']$ and using (8) then

$$\begin{aligned}\mathrm{E}\left[\tilde{\boldsymbol{e}}_{i,\mathrm{d}}[k]\tilde{\boldsymbol{e}}_{i,\mathrm{d}}^*[k']\right] &= \sum_{l=0}^{L-1}\sum_{\substack{q\in\mathcal{K}_{\rm on}\\ q\neq k}} E_q\rho[l,k-q]\delta[k-k'] \\ &= \sigma_d^2[k]\delta[k-k'].\end{aligned} \tag{12}$$

Thus, the Doppler interference is assumed uncorrelated. However, the variance $\sigma_d^2[k] = \mathrm{E}\left[|\tilde{\boldsymbol{e}}_{i,\mathrm{d}}[k]|^2\right]$ depends on the subcarrier index. Noting that

$$\tilde{\boldsymbol{h}}_i[k] = \frac{1}{K}\sum_{l=0}^{L-1}\bar{\boldsymbol{h}}_i[l,0]e^{-j2\pi\frac{kl}{K}}, \tag{13}$$

then, the channel gain and Doppler interference are uncorrelated, i.e. $\mathrm{E}\left[\tilde{\boldsymbol{h}}_i[k]\tilde{\boldsymbol{e}}_{i,\mathrm{d}}^*[k]\right] = 0$. Moreover, $\tilde{\boldsymbol{h}}_i[k]$ can be estimated from L uncorrelated taps defined by $\bar{\boldsymbol{h}}_i[l,0]$.

C. IEEE 802.11P VEHICULAR CHANNEL MODELS

As we have discussed, the wireless channel in vehicular environments is considered a time-varying channel including multi-path propagation and large Doppler shift [16]. Various studies that analyze the statistical characteristics of the wireless channel in vehicular environments are presented in [17], [18], and [19]. In this paper, we consider the tapped delay line (TDL) vehicular channel models proposed in [20]. These TDL models include six vehicular channel models for different vehicular environments. They are obtained by a measurement campaign that was implemented in metropolitan Atlanta. Table 3 provides the different characteristics of these vehicular channel models. Moreover, further investigations and discussion concerning the detailed channel models measurement setups are shown in [21].

III. CONVENTIONAL CHANNEL ESTIMATION SCHEMES

In this section, conventional channel estimators that adhere to the IEEE 802.11p standard structure are presented and discussed. These estimators assume that the allocated four pilots within each OFDM symbol are insufficient for accurately tracking the time variations of the vehicular channel. Therefore, they employ the data subcarriers in the channel estimation. DPA estimation is considered as an initial estimation, where the previously estimated channel is considered as a preamble to estimate the channel for the current received symbol. The STA estimation applies frequency and time averaging to the DPA estimated channel, while the E-TRFI estimation considers frequency domain interpolation to improve the DPA estimation.

A. DPA ESTIMATOR

The DPA estimator is based on employing the demapped data subcarriers of the previously received OFDM symbol to estimate the channel for the current OFDM symbol according to the following steps

1) **LS estimation**: that is implemented using the two LTS received preambles denoted as $\tilde{\boldsymbol{y}}_1^{(p)}[k]$, and $\tilde{\boldsymbol{y}}_2^{(p)}[k]$, and the predefined preamble sequence $\tilde{\boldsymbol{p}}[k]$ such that

$$\hat{\tilde{\boldsymbol{h}}}_{\rm LS}[k] = \frac{\tilde{\boldsymbol{y}}_1^{(p)}[k] + \tilde{\boldsymbol{y}}_2^{(p)}[k]}{2\tilde{\boldsymbol{p}}[k]}. \tag{14}$$

2) **Equalization**: the i-th received OFDM symbol is equalized by the previously DPA estimated channel, such that

$$\tilde{\boldsymbol{y}}_{\mathrm{eq}_i}[k] = \frac{\tilde{\boldsymbol{y}}_i[k]}{\hat{\tilde{\boldsymbol{h}}}_{\mathrm{DPA}_{i-1}}[k]},\ \hat{\tilde{\boldsymbol{h}}}_{\mathrm{DPA}_0}[k] = \hat{\tilde{\boldsymbol{h}}}_{\rm LS}[k]. \tag{15}$$

3) **Demapping**: $\tilde{\boldsymbol{y}}_{\mathrm{eq}_i}[k]$ is demapped to the nearest constellation point to obtain $\tilde{\boldsymbol{d}}_i[k]$.
4) **Final DPA estimation**: DPA updates the final estimated channel for the i-th received OFDM symbol by

$$\hat{\tilde{\boldsymbol{h}}}_{\mathrm{DPA}_i}[k] = \frac{\tilde{\boldsymbol{y}}_i[k]}{\tilde{\boldsymbol{d}}_i[k]}. \tag{16}$$

DPA scheme is considered as the initial estimation process utilized by most IEEE 802.11p conventional estimators. However, DPA estimation has two main limitations. First, it is based on the basic $\hat{\tilde{\boldsymbol{h}}}_{\rm LS}$ estimation suffering from noise enhancement. Second, the demapping step in DPA results in a significant demapping error mainly in low SNR region, and this error is enlarged in high mobility vehicular scenarios

TABLE 3: Vehicular channel models characteristics following Jake's Doppler spectrum.

Channel model	Channel taps	Vehicle velocity [kmph]	Max Doppler shift [Hz]	Average path gains [dB]	Path delays [ns]
RTV-SS	12	32-48	500	[0, 0, -9.3, -9.3, -14, -14, -18, -18, -19.4, -24.9, -27.5, -29.8]	[0, 1, 100, 101, 200, 201, 300,301, 400, 500, 600, 700]
RTV-EX	12	104	700	[0, 0, 0, -9.3, -9.3, -9.3, -20.3, -20.3, -21.3, -21.3, -28.8, -28.8]	[0, 1, 2, 100, 101, 102, 200, 201, 300, 301, 400, 401]
RTV-UC	12	32-48	300	[0, 0, 0, -11.5, -11.5, -11.5, -19, -19, -25.6, -25.6, -28.1, -28.1]	[0, 1, 2, 100, 101, 102, 200, 201, 300, 301, 500, 501]
VTV-EX	11	104	1200	[0, 0, 0, -6.3, -6.3, -25.1, -25.1, -25.1, -22.7, -22.7, -22.7]	[0, 1, 2, 100, 101, 200, 201, 202, 300, 301, 302]
VTV-UC	12	32-48	500	[0, 0, -10, -10, -10, -17.8, -17.8, -17.8, -21.1, -21.1, -26.3, -26.3]	[0, 1, 100, 101, 102, 200, 201, 202, 300, 301, 400, 401]
VTV-SDWW	12	104	1150	[0, 0, -11.2, -11.2, -19, -21.9, -25.3, -25.3, -24.4, -28, -26.1, -26.1]	[0, 1, 100, 101, 200, 300, 400, 401, 500, 600, 700, 701]

employing high modulation orders. Moreover, since the DPA estimated channels are updated iteratively over the received frame, the demapping error propagates through the frame leading to significant performance degradation.

B. STA ESTIMATOR

The STA estimator [7] has been proposed to further improve the DPA estimation by applying two additional steps on top of the DPA estimation. The first step is by performing frequency domain averaging to the DPA estimated channel including the current and the neighboring subcarriers as follows

$$\hat{\tilde{\boldsymbol{h}}}_{\mathrm{FD}_i}[k] = \sum_{\lambda=-\beta}^{\lambda=\beta} \omega_\lambda \hat{\tilde{\boldsymbol{h}}}_{\mathrm{DPA}_i}[k+\lambda],\ \omega_\lambda = \frac{1}{2\beta+1}, \quad (17)$$

After that, the final STA channel estimate is updated using time averaging between the previously STA estimated channel and the frequency averaged channel in (17), such that

$$\hat{\tilde{\boldsymbol{h}}}_{\mathrm{STA}_i}[k] = (1-\frac{1}{\alpha})\hat{\tilde{\boldsymbol{h}}}_{\mathrm{STA}_{i-1}}[k] + \frac{1}{\alpha}\hat{\tilde{\boldsymbol{h}}}_{\mathrm{FD}_i}[k]. \quad (18)$$

STA estimator performs well in low SNR region. However, it suffers from a considerable error floor in high SNR region because of large DPA demapping error. It is worth mentioning that in order to improve the STA performance, the optimal values of the frequency and time averaging coefficients denoted by α and β should be estimated according to channel statistics so that α and β can be adapted to the channel model. Channel model statistics are hard to obtain in real case scenarios, therefore, α and β are considered as fixed values that are chosen experimentally to achieve the best acceptable performance.

C. E-TRFI ESTIMATOR

Recently, the authors in [11] proposed the E-TRFI estimator that is considered as an upgraded version of the conventional TRFI estimator [10]. The main E-TRFI upgrades are in the reliable and unreliable subcarriers selection algorithm, where the Euclidean distance between the demapped subcarriers is used as a reliability condition. Moreover, E-TRFI employs the estimated channels at the $\mathcal{K}_{\mathrm{n}}$ subcarriers in order to improve the cubic interpolation accuracy. The E-TRFI estimator proceeds as follows:

1) **Enhanced LS estimation**: The conventional LS estimation presented in (14) estimates the channel at $\mathcal{K}_{\mathrm{on}}$ subcarriers. However, the E-TRFI employs the estimated channel also at the remaining $\mathcal{K}_{\mathrm{n}}$ subcarriers that are interpolated as follows

$$\hat{\tilde{\boldsymbol{h}}}_{\mathrm{E\text{-}LS}}[k] = \boldsymbol{F}_{64}(\boldsymbol{F}_{52}^{\mathrm{H}}\boldsymbol{F}_{52})^{-1}\boldsymbol{F}_{52}^{\mathrm{H}}\hat{\tilde{\boldsymbol{h}}}_{\mathrm{LS}}[k],\ k \in \mathcal{K}, \quad (19)$$

where $\boldsymbol{F}_{64} \in \mathbb{C}^{K\times L}$ and $\boldsymbol{F}_{52} \in \mathbb{C}^{K_{\mathrm{on}}\times L}$ denote the truncated DFT matrix obtained by selecting K, K_{on} rows, and L columns from the $K \times K$ DFT matrix,

respectively. Here, L represents the number of channel taps.

2) **Equalization**: The i-th received OFDM symbol is equalized by $\hat{\tilde{\boldsymbol{h}}}_{\text{E-TRFI}_{i-1}}[k]$, where

$$\tilde{\boldsymbol{y}}'_{\text{eq}_i}[k] = \frac{\tilde{\boldsymbol{y}}_i[k]}{\hat{\tilde{\boldsymbol{h}}}_{\text{E-TRFI}_{i-1}}[k]}, k \in \mathcal{K}_\text{d}. \tag{20}$$

Here, $\hat{\tilde{\boldsymbol{h}}}_{\text{E-TRFI}_0}[k] = \hat{\tilde{\boldsymbol{h}}}_{\text{E-LS}}[k]$. After that, the obtained $\tilde{\boldsymbol{y}}'_{\text{eq}_i}[k]$ is demapped to the nearest constellation point denoted as $\tilde{\boldsymbol{d}}'_i[k]$.

3) **Euclidean distance reliability test**: In order to ensure that $\tilde{\boldsymbol{d}}'_i[k]$ is correctly demapped, the E-TRFI estimator employs a reliability test where the Euclidean distances between $\tilde{\boldsymbol{y}}'_{\text{eq}_i}[k]$ and the constellation points are calculated such that

$$\boldsymbol{\delta}_i^{(m)}[k] = |\tilde{\boldsymbol{y}}'_{\text{eq}_i}[k] - \boldsymbol{c}^{(m)}|^2, \ m = 1, 2, \ldots, M. \tag{21}$$

$\boldsymbol{c}^{(m)}$ denotes the m-th constellation point with M standing for the employed modulation order. The obtained $\boldsymbol{\delta}_i^{(m)}[k]$ values are arranged in ascending order vector denoted as $\bar{\boldsymbol{\delta}}_i^{(m)}[k]$, then the reliability ratio for each subcarrier $\boldsymbol{R}_i[k]$ is calculated employing the first and second minimum distances as follows

$$\boldsymbol{R}_i[k] = \frac{\bar{\boldsymbol{\delta}}_i^{(1)}[k]}{\bar{\boldsymbol{\delta}}_i^{(2)}[k]}, \ k \in \mathcal{K}_\text{d}, \tag{22}$$

where $0 < \boldsymbol{R}_i[k] < 1$. Small $\boldsymbol{R}_i[k]$ value indicates that the demapped subcarrier $\tilde{\boldsymbol{d}}'_i[k]$ is close to actual transmitted modulated symbol. Therefore, the subcarrier is classified as a reliable subcarrier and inserted into the reliable subcarriers set $\mathcal{RS}_i$, otherwise, it is considered unreliable and inserted into the unreliable subcarriers set $\mathcal{URS}_i$. The extensive simulations performed in [11], show that $\boldsymbol{R}_i[k] = 0.5$ is the best-predefined threshold for the reliability test.

4) **Frequency domain cubic interpolation**: After selecting the $\mathcal{RS}_i$ and $\mathcal{URS}_i$ sets, frequency-domain cubic interpolation [22] is applied by using the channel estimates in $\mathcal{RS}_i$ to determine the channel estimates for the $\mathcal{URS}_i$, such that

$$\hat{\tilde{\boldsymbol{h}}}_{\text{Int}_i}[k] = \begin{cases} \tilde{\boldsymbol{y}}_i[k]/\tilde{\boldsymbol{d}}'_i[k], & k \in \mathcal{RS}_i. \\ \tilde{\boldsymbol{y}}_i[k]/\tilde{\boldsymbol{x}}_{\text{p}_i}[k], & k \in \mathcal{K}_\text{p}. \\ \tilde{\boldsymbol{y}}_i[k]/\hat{\tilde{\boldsymbol{h}}}_{\text{E-TRFI}_{i-1}}[k], & k \in \mathcal{K}_\text{n}. \\ \text{Cubic Interpolation}, & k \in \mathcal{URS}_i. \end{cases} \tag{23}$$

5) **Noise attenuation**: The last step in the E-TRFI estimator is applying a noise attenuation as follows

$$\hat{\tilde{\boldsymbol{h}}}_{\text{E-TRFI}_i}[k] = \boldsymbol{Q}\hat{\tilde{\boldsymbol{h}}}_{\text{Int}_i}[k], \ k \in \mathcal{K}, \tag{24}$$

where $\boldsymbol{Q} = \boldsymbol{F}_{64}\boldsymbol{F}_{64}^{\text{H}}$. We note that the computation of $\boldsymbol{Q}$ depends mainly on the L channel taps and it can be performed offline resulting in reducing the computational complexity.

The E-TRFI estimator outperforms other conventional estimators, however, it still suffers from a considerable performance degradation due to the enlarged demapping error in high mobility scenarios, and high computational complexity due to the matrix multiplication in (19) and (24). Moreover, the Euclidean distance reliability test threshold should be updated in a real-time manner in order to guarantee the best possible performance.

D. LMMSE ESTIMATOR

The LMMSE estimator [12] aims to linearly minimize the mean squared error (MSE) error between the LMMSE estimated and real channel, given the LS estimated channel at the $\mathcal{K}_\text{p}$ subcarriers defined as

$$\hat{\tilde{\boldsymbol{h}}}_{p_i}[k] = \frac{\tilde{\boldsymbol{y}}_{p_i}[k]}{\tilde{\boldsymbol{x}}_{p_i}[k]}, \ k \in \mathcal{K}_\text{p}. \tag{25}$$

Accordingly, the key element here is to find $\boldsymbol{W}_{\text{LMMSE}_i}$ where $\hat{\boldsymbol{h}}_{\text{LMMSE}_i} = \boldsymbol{W}_{\text{LMMSE}_i}\hat{\tilde{\boldsymbol{h}}}_{p_i}$, so that $\boldsymbol{\epsilon}_{\text{LMMSE}}$ is minimized, such that

$$\boldsymbol{\epsilon}_{\text{LMMSE}} = \text{E}\left[(\hat{\boldsymbol{h}}_{\text{LMMSE}_i} - \tilde{\boldsymbol{h}}_i)^2\right] = \text{E}\left[(\boldsymbol{W}_{\text{LMMSE}_i}\hat{\tilde{\boldsymbol{h}}}_{p_i} - \tilde{\boldsymbol{h}}_i)^2\right]. \tag{26}$$

The minimization of $\boldsymbol{\epsilon}_{\text{LMMSE}}$ results in the following expression

$$\boldsymbol{W}_{\text{LMMSE}_i} = \boldsymbol{R}_{\tilde{\boldsymbol{h}}_i\tilde{\boldsymbol{h}}_{p_i}}\left(\boldsymbol{R}_{\tilde{\boldsymbol{h}}_{p_i}\tilde{\boldsymbol{h}}_{p_i}} + \sigma^2\boldsymbol{I}'\right)^{-1}. \tag{27}$$

$\boldsymbol{R}_{\tilde{\boldsymbol{h}}_i,\tilde{\boldsymbol{h}}_{p_i}} = \text{E}\left[\tilde{\boldsymbol{h}}_i\tilde{\boldsymbol{h}}_{p_i}^H\right] \in \mathbb{C}^{K_d \times K_p}$ represents the cross correlation matrix of the real channel and the real channel vector at the $\mathcal{K}_\text{p}$ pilot subcarriers within the i-th received OFDM symbol. Moreover, $\boldsymbol{R}_{\tilde{\boldsymbol{h}}_{p_i},\tilde{\boldsymbol{h}}_{p_i}} = \text{E}\left[\tilde{\boldsymbol{h}}_{p_i}\tilde{\boldsymbol{h}}_{p_i}^H\right] \in \mathbb{C}^{K_p \times K_p}$ denotes the autocorrelation matrix of $\tilde{\boldsymbol{h}}_{p_i}$. I'_{K_p} is the identity matrix, and σ^2 is the noise power. Therefore, the LMMSE estimated channel at the $\mathcal{K}_\text{d}$ data subcarriers within the i-th received OFDM symbol can be simply obtained as follows

$$\hat{\tilde{\boldsymbol{h}}}_{\text{LMMSE}_i} = \boldsymbol{W}_{\text{LMMSE}_i}\hat{\tilde{\boldsymbol{h}}}_{p_i}. \tag{28}$$

It is worth mentioning that the LMMSE performance highly depends on the pre-estimated $\boldsymbol{W}_{\text{LMMSE}}$ matrix, where it suffers from considerable performance degradation in case the channel employed in the $\boldsymbol{W}_{\text{LMMSE}}$ estimation changes. Therefore, it is impractical to be employed in real-time scenarios.

IV. PROPOSED DFT-BASED CHANNEL ESTIMATION SCHEMES

In this section, a detailed description of the time-variant channel estimation problem is first given. After that, the classical DFT based estimator, the proposed T-DFT, and TA-TDFT estimators which adhere to the IEEE 802.11p standard are presented. Moreover, the analytical NMSE expressions of the proposed estimators are derived and compared.

As discussed, the wireless channel in vehicular environment is considered as a doubly selective channel, it is time selective due to the vehicle's motion, and frequency selective due to the multi-path fading impact on the transmitted OFDM frames. Recall (10)

$$\tilde{\boldsymbol{y}}_i[k] = \tilde{\boldsymbol{h}}_i[k]\tilde{\boldsymbol{x}}_i[k] + \tilde{\boldsymbol{e}}_{i,\mathrm{d}}[k] + \tilde{\boldsymbol{v}}_i[k],\ k \in \mathcal{K}_{\mathrm{on}}$$

where, $\tilde{\boldsymbol{h}}_i[k] = \frac{1}{K}\sum_{l=0}^{L-1} \bar{\boldsymbol{h}}_i[l,0]e^{-j2\pi\frac{kl}{K}}$. The goal is to estimate $\tilde{\boldsymbol{h}}_i[k]$ at the data subcarriers based on the pilot subcarriers. Let $\boldsymbol{h}_{i,L} \in \mathbb{C}^{L\times 1}$, defined by $\boldsymbol{h}_{i,L}[l] = \frac{1}{K}\bar{\boldsymbol{h}}_i[l,0], l = 0\cdots L-1$. Accordingly, the vector model corresponding to the $\mathcal{K}_{\mathrm{p}}$, and $\mathcal{K}_{\mathrm{d}}$ subcarriers can be expressed as follows

$$\begin{cases} \tilde{\boldsymbol{y}}_{p_i} &= (\boldsymbol{F}_p\boldsymbol{h}_{i,L}) \odot \tilde{\boldsymbol{x}}_{\mathrm{p}_i} + \tilde{\boldsymbol{e}}_{p_i,d} + \tilde{\boldsymbol{v}}_{p_i}, \quad k \in \mathcal{K}_{\mathrm{p}}. \\ \tilde{\boldsymbol{y}}_{d_i} &= (\boldsymbol{F}_d\boldsymbol{h}_{i,L}) \odot \tilde{\boldsymbol{x}}_{\mathrm{d}_i} + \tilde{\boldsymbol{e}}_{d_i,d} + \tilde{\boldsymbol{v}}_{d_i}, \quad k \in \mathcal{K}_{\mathrm{d}}. \end{cases} \tag{29}$$

where $\odot$ denotes the element-wise multiplication. $\boldsymbol{F}_d \in \mathbb{C}^{K_d\times L}$ represents the truncated DFT matrix obtained by selecting $\mathcal{K}_{\mathrm{d}}$ rows, and L columns from the $K \times K$ DFT matrix. $\boldsymbol{F}_p \in \mathbb{C}^{K_{\mathrm{p}}\times L}$ denotes the truncated DFT matrices at $\mathcal{K}_{\mathrm{p}}$ subcarriers. The pilot signal is used to estimate $\boldsymbol{h}_{i,L}$. First, by dividing over the pilots, we get

$$\begin{aligned} \hat{\tilde{\boldsymbol{h}}}_{p_i} &= \tilde{\boldsymbol{y}}_{p_i} \oslash \tilde{\boldsymbol{x}}_{\mathrm{p}_i} + \tilde{\boldsymbol{e}}_{p_i,d} \oslash \tilde{\boldsymbol{x}}_{\mathrm{p}_i} + \tilde{\boldsymbol{v}}_{p_i} \oslash \tilde{\boldsymbol{x}}_{\mathrm{p}_i} \\ &= \tilde{\boldsymbol{h}}_{p_i} + \tilde{\boldsymbol{e}}_{p_i,d} \oslash \tilde{\boldsymbol{x}}_{\mathrm{p}_i} + \tilde{\boldsymbol{v}}_{p_i} \oslash \tilde{\boldsymbol{x}}_{\mathrm{p}_i}, \end{aligned} \tag{30}$$

where $\oslash$ is the element wise division, and $\tilde{\boldsymbol{h}}_{p_i} = \boldsymbol{F}_p\boldsymbol{h}_{i,L}$. In our work, we consider that the transmitted pilots are equal to one for simplicity. Moreover, after estimating $\hat{\boldsymbol{h}}_{i,L}$ employing $\hat{\tilde{\boldsymbol{h}}}_{p_i}$, the final channel estimate at K_d subcarriers of the i-th received OFDM symbol can be obtained according to the employed estimator as we will discuss in the next subsections, where $\tilde{\boldsymbol{h}}_{d_i} = \boldsymbol{F}_d\boldsymbol{h}_{i,L}$.

A. CLASSICAL DFT ESTIMATOR

The classical DFT estimator employs DFT interpolation [23] in order to obtain the final channel estimates at K_d subcarriers assuming that $\boldsymbol{F}_p$ is either tall or square matrix, i.e. $K_{\mathrm{p}} \geq L$. Therefore, $\hat{\boldsymbol{h}}_{i,L}$ can be estimated with the LS as

$$\hat{\boldsymbol{h}}_{i,L} = \boldsymbol{F}_p^{\dagger}\hat{\tilde{\boldsymbol{h}}}_{p_i} = \boldsymbol{h}_{i,L} + \boldsymbol{F}_p^{\dagger}(\tilde{\boldsymbol{e}}_{p_i,d} + \tilde{\boldsymbol{v}}_{p_i}). \tag{31}$$

Here, $\boldsymbol{F}_p^{\dagger} = (\boldsymbol{F}_p^{\mathrm{H}}\boldsymbol{F}_p)^{-1}\boldsymbol{F}_p^{\mathrm{H}}$ is the pseudo inverse matrix of $\boldsymbol{F}_p$, and $(\cdot)^{\mathrm{H}}$ denotes the conjugate transpose. After that, the estimate at the data subcarrier denoted as $\hat{\tilde{\boldsymbol{h}}}_{\mathrm{DFT}_i}$, is computed as follows

$$\hat{\tilde{\boldsymbol{h}}}_{\mathrm{DFT}_i} = \boldsymbol{F}_d\hat{\boldsymbol{h}}_{i,L} = \boldsymbol{F}_d\boldsymbol{h}_{i,L} + \boldsymbol{W}_{\mathrm{DFT}}\boldsymbol{z}_{\mathrm{DFT}_i}, \tag{32}$$

where $\boldsymbol{W}_{\mathrm{DFT}} = \boldsymbol{F}_d\boldsymbol{F}_p^{\dagger}$ denotes the DFT interpolation matrix and $\boldsymbol{z}_{\mathrm{DFT}_i} = \tilde{\boldsymbol{e}}_{p_i,d} + \tilde{\boldsymbol{v}}_{p_i}$. The DFT estimation MSE $\boldsymbol{\epsilon}_{\mathrm{DFT}}$ can be expressed as

$$\begin{aligned} \epsilon_{\mathrm{DFT}_i} &= \mathrm{E}\left[\left\|\hat{\tilde{\boldsymbol{h}}}_{\mathrm{DFT}_i} - \tilde{\boldsymbol{h}}_{i,d}\right\|^2\right] \\ &= \mathrm{trace}\left\{\boldsymbol{W}_{\mathrm{DFT}}\left(\boldsymbol{\Lambda}_{p,d} + \sigma^2\boldsymbol{I}_{K_p}\right)\boldsymbol{W}_{\mathrm{DFT}}^{\mathrm{H}}\right\}, \end{aligned} \tag{33}$$

where σ^2 denotes the noise variance, $\boldsymbol{\Lambda}_{p,d} = \mathrm{E}\left[\tilde{\boldsymbol{e}}_{p_i,d}\tilde{\boldsymbol{e}}_{p_i,d}^{\mathrm{H}}\right] \in \mathbb{C}^{K_p\times K_p}$ is the auto-correlation matrix of the Doppler error at $\mathcal{K}_{\mathrm{p}}$ subcarriers, and $\boldsymbol{I}_{K_p} \in \mathbb{C}^{K_p\times K_p}$ denotes the identity matrix. Based on (12), $\boldsymbol{\Lambda}_{p,d}$ is diagonal and independent of i.

B. PROPOSED TRUNCATED DFT ESTIMATOR FOR IEEE 802.11P STANDARD

Vehicular channel models consist of 12 taps, as discussed in [20], while the IEEE 802.11p standard allocates only four pilots for each transmitted OFDM symbol. However, considering the bandwidth of 10 MHz, the number of discrete significant taps is smaller as shown in Figure 2. Thus, classical DFT cannot be implemented in IEEE 802.11p standard, since the condition $K_{\mathrm{p}} \geq L$ is not satisfied. To overcome this limitation, we propose a T-DFT estimator that targets the estimation of only $L_{\mathrm{d}} = K_{\mathrm{p}}$ dominant channel taps out of L. The indexes of those dominant taps are denoted as $\mathcal{L}_{\mathrm{d}}$, $L_d = |\mathcal{L}_{\mathrm{d}}|$, and they are selected based on the maximum values of the channel impulse response amplitude denoted as $\rho[l,0]$ according to the measured channel profile as shown in Figure 2. The remaining minor taps are represented by the set $\mathcal{L}_{\mathrm{e}}$, $L_e = |\mathcal{L}_{\mathrm{e}}|$ and they are considered as noise. Thus, $\mathcal{L}_{\mathrm{d}} \cup \mathcal{L}_{\mathrm{e}} = \{0,\cdots,L-1\}$. Accordingly, let $\boldsymbol{h}_{i,\mathcal{L}_{\mathrm{d}}} \in \mathbb{C}^{L_d\times 1}$ and $\boldsymbol{h}_{i,\mathcal{L}_{\mathrm{e}}} \in \mathbb{C}^{L_e\times 1}$ be the vectors corresponding to the significant and minor channel taps, then the pilot signal (30) can be rewritten as

$$\hat{\tilde{\boldsymbol{h}}}_{i,p} = \boldsymbol{F}_{d,p}\boldsymbol{h}_{i,\mathcal{L}_{\mathrm{d}}} + \boldsymbol{F}_{e,p}\boldsymbol{h}_{i,\mathcal{L}_{\mathrm{e}}} + \tilde{\boldsymbol{e}}_{p_i,d} + \tilde{\boldsymbol{v}}_{p_i}, \tag{34}$$

where $\boldsymbol{F}_{d,p} \in \mathbb{C}^{K_{\mathrm{p}}\times L_d}$, $\boldsymbol{F}_{e,p} \in \mathbb{C}^{K_{\mathrm{p}}\times L_e}$ denote the truncated DFT matrices at $\mathcal{K}_{\mathrm{p}}$ subcarriers, and $\mathcal{L}_{\mathrm{d}}$, $\mathcal{L}_{\mathrm{e}}$ channel taps respectively, as shown in Figure 3. Similarly, the channel gain at the data subcarriers can be expressed as

$$\tilde{\boldsymbol{h}}_{i,d} = \boldsymbol{F}_d\boldsymbol{h}_{i,\mathcal{L}_{\mathrm{d}}} + \boldsymbol{F}_e\boldsymbol{h}_{i,\mathcal{L}_{\mathrm{e}}}. \tag{35}$$

Here $\boldsymbol{F}_d \in \mathbb{C}^{K_d\times L_d}$, and $\boldsymbol{F}_e \in \mathbb{C}^{K_d\times L_e}$ denote the truncated DFT matrices obtained by selecting its $\mathcal{K}_{\mathrm{d}}$ rows and $\mathcal{L}_{\mathrm{d}}$, $\mathcal{L}_{\mathrm{e}}$ columns respectively.

First, $\boldsymbol{h}_{i,\mathcal{L}_{\mathrm{d}}}$ is estimated using LS as

$$\begin{aligned} \hat{\boldsymbol{h}}_{i,\mathcal{L}_{\mathrm{d}}} &= \boldsymbol{F}_{d,p}^{\dagger}\hat{\tilde{\boldsymbol{h}}}_{i,p} \\ &= \boldsymbol{h}_{i,\mathcal{L}_{\mathrm{d}}} + \boldsymbol{F}_{d,p}^{\dagger}\boldsymbol{F}_{e,p}\boldsymbol{h}_{i,\mathcal{L}_{\mathrm{e}}} + \boldsymbol{F}_{d,p}^{\dagger}(\tilde{\boldsymbol{e}}_{p_i,d} + \tilde{\boldsymbol{v}}_{p_i}), \end{aligned} \tag{36}$$

where $\boldsymbol{F}_{d,p}^{\dagger}$ is the pseudo inverse matrix of $\boldsymbol{F}_{d,p}$. Therefore, the T-DFT estimator for IEEE 802.11p standard can be expressed as follows

$$\hat{\tilde{\boldsymbol{h}}}_{\text{T-DFT}_i} = \boldsymbol{F}_d\hat{\boldsymbol{h}}_{i,\mathcal{L}_{\mathrm{d}}} = \boldsymbol{F}_d\boldsymbol{h}_{i,\mathcal{L}_{\mathrm{d}}} + \boldsymbol{W}_{\mathrm{TDFT}}\boldsymbol{z}_{\mathrm{TDFT}_i}, \tag{37}$$

where $\boldsymbol{W}_{\mathrm{TDFT}_i} = \boldsymbol{F}_d\boldsymbol{F}_{d,p}^{\dagger}$ denotes the T-DFT interpolation matrix and $\boldsymbol{z}_{\mathrm{TDFT}_i} = \boldsymbol{F}_{e,p}\boldsymbol{h}_{i,\mathcal{L}_{\mathrm{e}}} + \tilde{\boldsymbol{e}}_{p_i,d} + \tilde{\boldsymbol{v}}_{p_i}$. The overall estimation error between $\tilde{\boldsymbol{h}}_{i,d}$ and $\hat{\tilde{\boldsymbol{h}}}_{\text{T-DFT}_i}$ is denoted by $\hat{e}_{\mathrm{TDFT}}$ and it can be expressed as follows

$$\begin{aligned} \boldsymbol{e}_{\mathrm{TDFT}} &= \hat{\tilde{\boldsymbol{h}}}_{\text{T-DFT}_i} - \tilde{\boldsymbol{h}}_{i,d} \\ &= \boldsymbol{W}_{\mathcal{L}_{\mathrm{e}}}\boldsymbol{h}_{i,\mathcal{L}_{\mathrm{e}}} + \boldsymbol{W}_{\mathrm{TDFT}}(\tilde{\boldsymbol{e}}_{p_i,d} + \tilde{\boldsymbol{v}}_{p_i}), \end{aligned} \tag{38}$$

where $\boldsymbol{W}_{\mathcal{L}_{\mathrm{e}}} = \boldsymbol{W}_{\mathrm{TDFT}}\boldsymbol{F}_{e,p} - \boldsymbol{F}_e$. Therefore, the T-DFT MSE

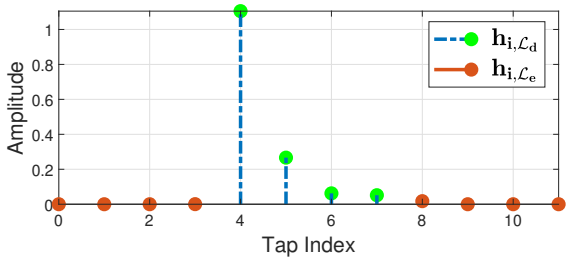

FIGURE 2: Vehicular channel dominant taps selection.

can be expressed as

$$\begin{aligned}\epsilon_{\text{T-DFT}} = \mathrm{E}\left[\left\|\boldsymbol{e}_{\text{TDFT}_i}\right\|^2\right] &= \mathrm{trace}\left\{\boldsymbol{W}_{\mathcal{L}_\mathrm{e}}\boldsymbol{\Lambda}_{\mathcal{L}_\mathrm{e}}\boldsymbol{W}_{\mathcal{L}_\mathrm{e}}^{\mathrm{H}}\right\} \\ &+ \mathrm{trace}\left\{\boldsymbol{W}_{\text{TDFT}}\left(\boldsymbol{\Lambda}_{p,d}+\sigma^2\boldsymbol{I}_{K_p}\right)\boldsymbol{W}_{\text{TDFT}}^{\mathrm{H}}\right\},\end{aligned} \tag{39}$$

where $\boldsymbol{\Lambda}_{\mathcal{L}_\mathrm{e}} = \mathrm{E}\left[\boldsymbol{h}_{i,\mathcal{L}_\mathrm{e}}\boldsymbol{h}_{i,\mathcal{L}_\mathrm{e}}{}^{\mathrm{H}}\right] \in \mathbb{C}^{L_e\times L_e}$ represents the auto-correlation matrix of the $\mathcal{L}_\mathrm{e}$ neglected channel taps, which is independent of i. Note that, $\boldsymbol{\Lambda}_{\mathcal{L}_\mathrm{e}}$ is diagonal and $\mathrm{E}\left[\tilde{\boldsymbol{e}}_{p_i,d}\boldsymbol{h}_{i,\mathcal{L}_\mathrm{e}}^{\mathrm{H}}\right] = \boldsymbol{0}$ due to the uncorrelated Delay-Doppler assumption. The classical DFT estimation is a special case when all the taps are considered. Thus, the error term $\mathrm{trace}\left\{\boldsymbol{W}_{\mathcal{L}_\mathrm{e}}\boldsymbol{\Lambda}_{\mathcal{L}_\mathrm{e}}\boldsymbol{W}_{\mathcal{L}_\mathrm{e}}^{\mathrm{H}}\right\}$ is null, and the interpolation matrix $\boldsymbol{W}_{\text{TDFT}}$ becomes $\boldsymbol{W}_{\text{DFT}}$.

C. PROPOSED TEMPORAL AVERAGING T-DFT ESTIMATOR

Considering the high temporal correlation between the successive channels, $\tilde{\boldsymbol{h}}_{i,d}$ and $\tilde{\boldsymbol{h}}_{i+1,d}$, averaging has the potential of improving the estimation gradually. To demonstrate that, let $\tilde{\boldsymbol{h}}_{i,d} = \tilde{\boldsymbol{h}}_d + \tilde{\boldsymbol{\epsilon}}_i$, where $\tilde{\boldsymbol{h}}_d$ is static and $\tilde{\boldsymbol{\epsilon}}_i$ denotes the variation. Similarly, $\boldsymbol{h}_{i,\mathcal{L}_\mathrm{e}} = \boldsymbol{h}_{\mathcal{L}_\mathrm{e}} + \boldsymbol{\Delta}_{i,\mathcal{L}_\mathrm{e}}$. Thus, using (38), we get

$$\hat{\tilde{\boldsymbol{h}}}_{\text{T-DFT}_i} = \tilde{\boldsymbol{h}}_d + \underbrace{\boldsymbol{W}_{\mathcal{L}_\mathrm{e}}\boldsymbol{h}_{\mathcal{L}_\mathrm{e}}}_{\boldsymbol{c}} + \underbrace{\tilde{\boldsymbol{\epsilon}}_i + \boldsymbol{W}_{\mathcal{L}_\mathrm{e}}\boldsymbol{\Delta}_{i,\mathcal{L}_\mathrm{e}}}_{\boldsymbol{z}_i} + \underbrace{\boldsymbol{W}_{\text{TDFT}}(\tilde{\boldsymbol{e}}_{p_i,d}+\tilde{\boldsymbol{v}}_{p_i})}_{\boldsymbol{\eta}_i}$$

Note that $\tilde{\boldsymbol{e}}_{p_i,d}\tilde{\boldsymbol{e}}_{p_j,d}^{H} = \delta[i-j]\boldsymbol{\Lambda}_{p,d}$, due to the assumption of uncorrelated data, and $\mathrm{E}\left[\tilde{\boldsymbol{v}}_{p_i}\tilde{\boldsymbol{v}}_{p_j}^{H}\right] = \delta[i-j]\sigma^2\boldsymbol{I}_{K_p}$. Therefore, $\boldsymbol{\eta}_i = \boldsymbol{W}_{\text{TDFT}}(\tilde{\boldsymbol{e}}_{p_i,d}+\tilde{\boldsymbol{v}}_{p_i})$ is the error term that benefits from averaging. On the other hand, the term $\boldsymbol{z}_i = \tilde{\boldsymbol{\epsilon}}_i + \boldsymbol{W}_{\mathcal{L}_\mathrm{e}}\boldsymbol{\Delta}_{i,\mathcal{L}_\mathrm{e}}$ is a correlated error term, whereas $\boldsymbol{c} = \boldsymbol{W}_{\mathcal{L}_\mathrm{e}}\boldsymbol{h}_{\mathcal{L}_\mathrm{e}}$ is a static error within the frame. Both terms do not benefit from the averaging.

The TA-TDFT can be achieved such that

$$\hat{\tilde{\boldsymbol{h}}}_{\text{TA-TDFT}_i} = \begin{cases} \hat{\tilde{\boldsymbol{h}}}_{\text{T-DFT}_i}, & i = 1 \\ \gamma\hat{\tilde{\boldsymbol{h}}}_{\text{TA-TDFT}_{i-1}} + (1-\gamma)\hat{\tilde{\boldsymbol{h}}}_{\text{T-DFT}_i}, & 2 \leqslant i \leqslant I \end{cases} \tag{40}$$

where γ defines the weights given to $\hat{\tilde{\boldsymbol{h}}}_{\text{TA-TDFT}_{i-1}}$ and $\hat{\tilde{\boldsymbol{h}}}_{\text{T-DFT}_i}$. In our simulations we consider $\gamma = \frac{1}{2}$, therefore $\hat{\tilde{\boldsymbol{h}}}_{\text{TA-TDFT}_i}$ can be rewritten in terms of the previous estimated T-DFT channels $\hat{\tilde{\boldsymbol{h}}}_{\text{T-DFT}_i}$ as follows

$$\begin{aligned}\hat{\tilde{\boldsymbol{h}}}_{\text{TA-TDFT}_i} &= \left(\frac{1}{2}\right)^{(i-1)}\hat{\tilde{\boldsymbol{h}}}_{\text{T-DFT}_1} + \sum_{j=2}^{i}\left(\frac{1}{2}\right)^{(i-j+1)}\hat{\tilde{\boldsymbol{h}}}_{\text{T-DFT}_j} \\ &= \left[\tilde{\boldsymbol{h}}_d + \tilde{\boldsymbol{\epsilon}}_i\right] + \boldsymbol{c} + \left[\boldsymbol{z}_{\text{TA-TDFT}_i} - \tilde{\boldsymbol{\epsilon}}_i\right] + \boldsymbol{\eta}_{\text{TA-TDFT}_i}.\end{aligned} \tag{41}$$

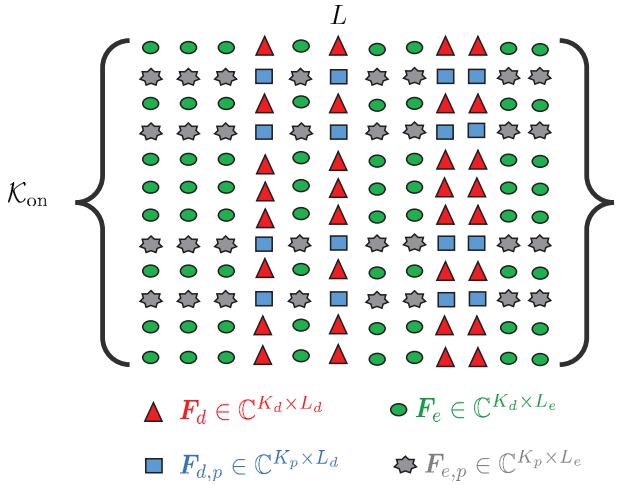

FIGURE 3: Proposed T-DFT truncated DFT matrices.

Here, the overall error terms are given by

$$\begin{aligned}\boldsymbol{z}_{\text{TA-TDFT}_i} &= \left(\frac{1}{2}\right)^{(i-1)}\boldsymbol{z}_1 + \sum_{j=2}^{i}\left(\frac{1}{2}\right)^{(i-j+1)}\boldsymbol{z}_j \\ \boldsymbol{\eta}_{\text{TA-TDFT}_i} &= \left(\frac{1}{2}\right)^{(i-1)}\boldsymbol{\eta}_1 + \sum_{j=2}^{i}\left(\frac{1}{2}\right)^{(i-j+1)}\boldsymbol{\eta}_j\end{aligned} \tag{42}$$

The TA-TDFT overall estimation error depends on the i-th received OFDM symbol, the SNR, and the Doppler. At low SNR, the estimation error is highly influenced by the noise, where $\boldsymbol{\eta}_i \approx \boldsymbol{W}_{\text{TDFT}}\tilde{\boldsymbol{v}}_{p_i}$. In this case, the averaging reduces the noise power when i increases, such that

$$\epsilon^{(1)}_{\text{TA-TDFT}_i} \leq \boldsymbol{N}_{\text{TA-TDFT}_i}\sigma^2\mathrm{trace}\left\{\boldsymbol{W}_{\text{TDFT}}\boldsymbol{W}_{\text{TDFT}}^{H}\right\}, \tag{43}$$

where

$$\boldsymbol{N}_{\text{TA-TDFT}_i} = \left(\frac{1}{4}\right)^{(i-1)} + \sum_{j=2}^{i}\left(\frac{1}{4}\right)^{(i-j+1)} = \frac{4^{i-1}+2}{3\times 4^{i-1}}. \tag{44}$$

At high SNR region and low mobility, the error is influenced by non-significant channel taps error $\boldsymbol{c}$, and thus,

$$\epsilon^{(2)}_{\text{TA-TDFT}_i} \leq \mathrm{trace}\left\{\boldsymbol{W}_{\text{TDFT}}\boldsymbol{\Lambda}_{\mathcal{L}_\mathrm{e}}\boldsymbol{W}_{\text{TDFT}}^{H}\right\}. \tag{45}$$

At high mobility, the error is influenced by $\boldsymbol{z}_{\text{TA-DFT}_i} - \tilde{\boldsymbol{\epsilon}}_i$, which leads to an increase of the averaging error because of the increase in $\|\tilde{\boldsymbol{\epsilon}}_i\|$. Accordingly, the gain of averaging is notable at low SNR, not significant at high SNR with low mobility, and worse at very high SNR and very high mobility. We note that $\epsilon^{(1)}_{\text{TA-TDFT}_i} + \epsilon^{(2)}_{\text{TA-TDFT}_i}$ denotes the lower bound

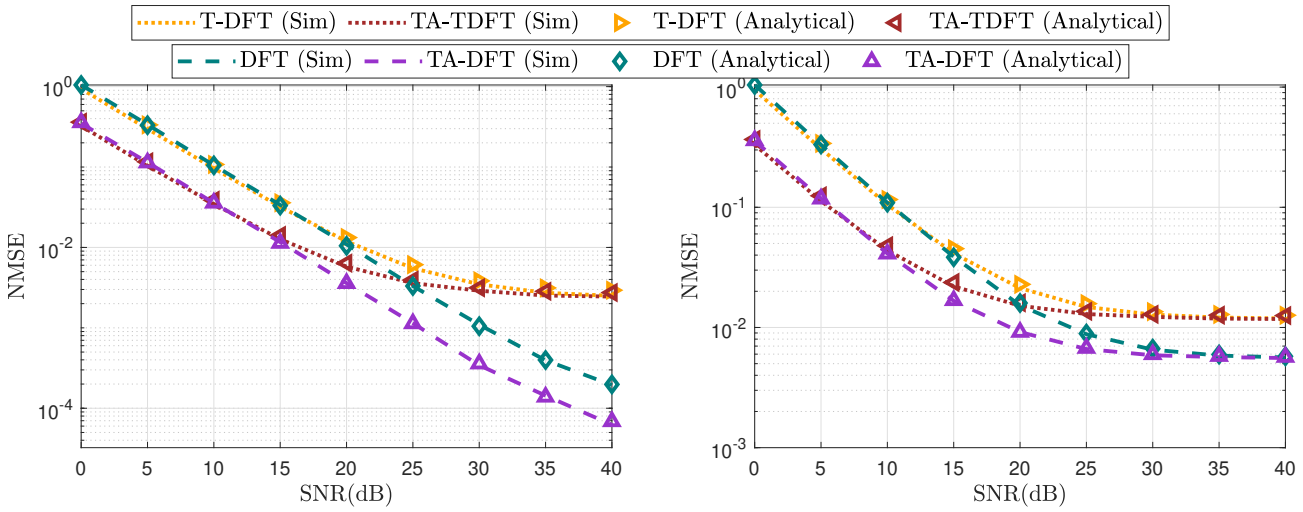

(a) Low mobility vehicular channel model.

(b) High mobility vehicular channel model.

FIGURE 4: NMSE analytical and simulation results for low and high mobility vehicular channel models respectively.

performance of the TA-TDFT estimator.

Figure 4 shows the analytical and simulated NMSE curves of the proposed estimators in low and high mobility vehicular scenarios. Moreover, the classical DFT and TA-DFT where the temporal averaging is employed with classical DFT estimation are also presented for better illustrating the performance degradation sources.

It can be noticed that the analytical results coincide with the simulated results, thus validating the derived NMSE expressions for the proposed estimators. It is clearly shown that applying temporal averaging on top of the T-DFT estimator improves the NMSE performance, especially in low SNR region, where the impact of noise is dominant. This is because adding the temporal averaging step to the T-DFT estimated channels, reduces the noise power iteratively over the frame, and thus the SNR increases resulting in improving the total channel estimation accuracy. On the other hand, the TA-TDFT estimator suffers from an error floor in high SNR region, due to the channel model error resulting from the neglected $\mathcal{L}_e$ channel taps in low mobility scenario, Figure 4a, in addition to Doppler interference error in high mobility scenario, Figure 4b. Moreover, employing TA-DFT estimator with $K_p = L = 12$ pilot subcarriers, leads to a significant NMSE performance improvement over the whole SNR region, especially in low mobility scenario, since L channel taps are estimated by the DFT estimator. However, it can be noticed that in high mobility scenario, the temporal averaging step is not helpful, especially in high SNR region even though the impact of noise is very low. But on the other hand, the dominant impact of Doppler interference error in high mobility scenarios affects the performance improvement caused by the temporal averaging step in high SNR region.

Finally, we note that if $K_p = 12$ is considered, this requires a modification in the IEEE 802.11p standard structure, where 1Mbps loss in the transmission data rates is recorded,

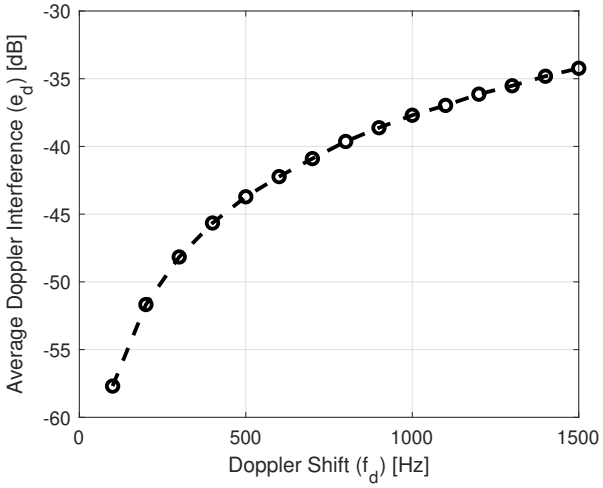

FIGURE 5: Doppler spectrum Interference.

since the data subcarriers K_d becomes 40 instead of 48 data subcarriers per OFDM symbol. However, in this paper, we focus on the estimators that adhere to the IEEE 802.11p standard, therefore, only T-DFT and TA-TDFT estimators will be considered in the simulations.

V. SIMULATION RESULTS

In this section, NMSE and BER simulations are conducted in order to evaluate the performance of the proposed estimators compared to IEEE 802.11p conventional estimators and the LMMSE estimator where three simulation scenarios are considered as follows

- Low mobility vehicular scenario, where the VTV-UC channel model is employed using V = 45 Kmph which is equivalent to $F_d = 250$ Hz as a maximum Doppler

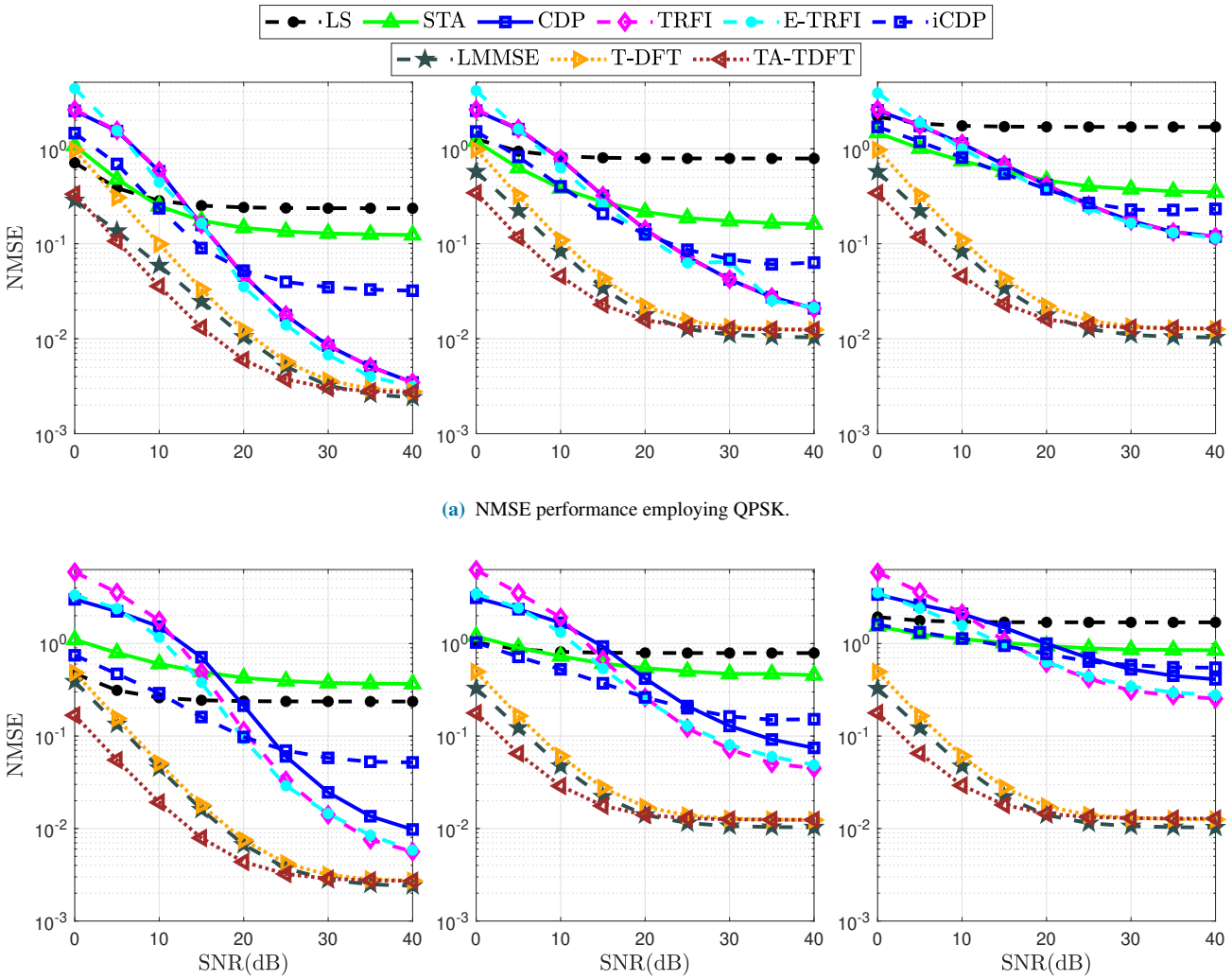

(a) NMSE performance employing QPSK.

(b) NMSE performance employing 16QAM.

FIGURE 6: NMSE performance employing three scenarios: (*i*) first column - low mobility ($v = 45$ Kmph, $f_d = 250$ Hz) (*ii*) second column - high mobility ($v = 100$ Kmph, $f_d = 500$ Hz) (*iii*) third column - very high mobility ($v = 200$ Kmph, $f_d = 1000$ Hz).

shift.

- High mobility vehicular scenario, where the VTV-SDWW channel model with V $=$ 100 Kmph and $F_d = 500$ Hz is employed.
- Very high mobility scenario, where the VTV-SDWW channel model is considered with V $=$ 200 Kmph and $F_d = 1000$ Hz. This scenario is employed in order to further evaluate the robustness of the proposed schemes.

We note that the NMSE is computed using the estimated channel $\tilde{\boldsymbol{h}}_{\Psi_i}$, where $\Psi \in \{\text{STA, CDP, } \dots\}$ and the power of the channel frequency-time response such that

$$\text{NMSE}_{\Psi} = \frac{\left\| \tilde{\boldsymbol{h}}_{\Psi_i} - \tilde{\boldsymbol{h}}_i \right\|^2}{\left\| \tilde{\boldsymbol{h}}_i \right\|^2}. \tag{46}$$

Moreover, two modulation orders are employed in the three simulation scenarios, QPSK and 16QAM. Moreover, convolutional channel coding with a $\frac{1}{2}$ code rate is used. The frame size is $I = 100$ OFDM symbols, and the SNR range $\in [0 \text{ dB}, 40 \text{ dB}]$. The NMSE and BER performance evaluation of the benchmarked estimators are performed over the chosen vehicular channel models according to three criteria: (i) Modulation order, (ii) Mobility, and (iii) frame length. Moreover, a robustness analysis is presented in order to evaluate the generalization ability of the proposed estimators in comparison to the LMMSE.

A. NMSE EVALUATION

As we can notice from Figure 6, the estimation error of the conventional DPA-based estimators are affected by the employed modulation order, where the estimation error increases for high modulation order. When short frame size is employed as shown in Figure 7a, the channel variation is negligible within the received OFDM frame. Therefore, we can

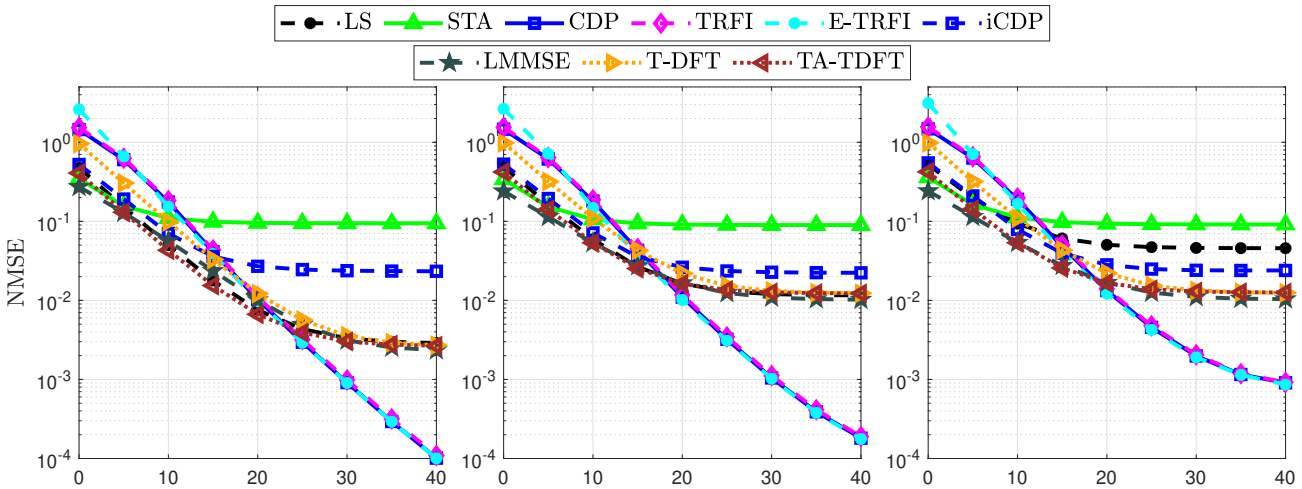

(a) NMSE performance with $I = 10$.

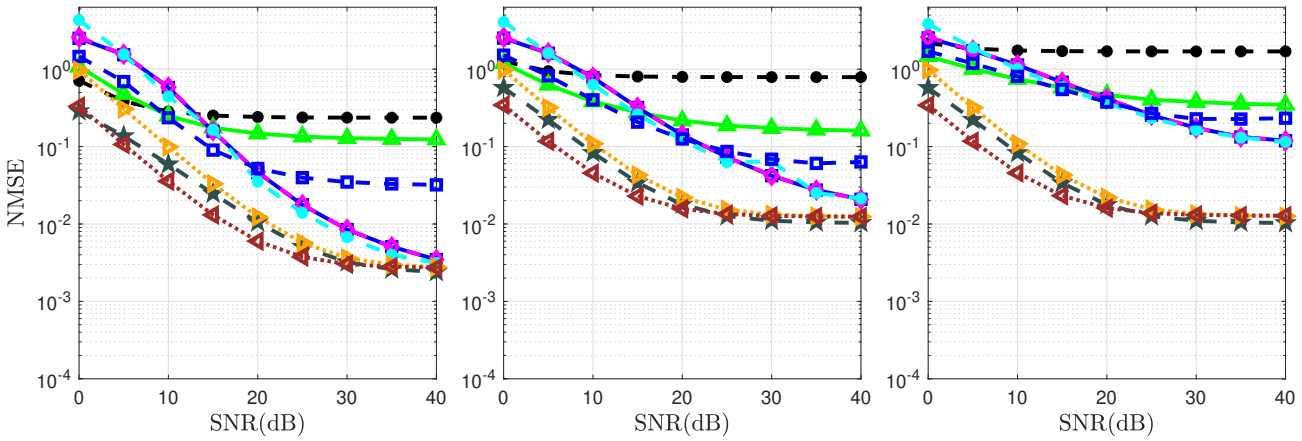

(b) NMSE performance with $I = 100$.

FIGURE 7: NMSE performance employing three scenarios: (*i*) first column - low mobility ($v = 45$ Kmph, $f_d = 250$ Hz) (*ii*) second column - high mobility ($v = 100$ Kmph, $f_d = 500$ Hz) (*iii*) third column - very high mobility ($v = 200$ Kmph, $f_d = 1000$ Hz).

notice that the performance degradation of the conventional DPA-based estimators is less than that when a longer frame is employed and the basic LS estimator still performs well, where it records similar performance as LMMSE especially in low SNR regions. However, in very high mobility scenarios, the impact of Doppler error is dominant, thus, affecting the performance of conventional DPA-based estimators. In contrast, we can notice that employing long frames leads to considerable performance challenges even in low mobility, where the basic LS estimator is not useful as shown in Figure 7b.

On the other hand, since the LMMSE and the proposed estimators are linear and do not employ demapping, then, the estimation error is independent of the modulation order. In addition, as the estimation is performed in symbol-by-symbol fashion, only TA-TDFT experiences dependency on the frame length since it employs averaging. This behavior can be seen in Figure 7. In particular, when the frame length is $I = 100$, the estimation error of TA-TDFT is slightly reduced at low mobility and low SNRs compared with shorter frames, as expected. In comparison with LMMSE , the T-DFT only approaches LMMSE at high SNR, whereas TA-TDFT outperforms LMMSE when the averaging is sufficient, which is the case of using a long frame ($I = 100$) at low SNRs, or in medium SNR region with a short frame ($I = 10$). However, at high mobility and high SNRs, the estimation error is influenced by Doppler interference as well as the channel model mismatch resulting from neglecting $\mathcal{L}_{\mathrm{e}}$ channel taps in the estimation process for all of the presented estimators. Figure 5 shows the average Doppler interference as f_{d} increases. For low mobility vehicular scenarios, where $f_{\mathrm{d}} < 200$ Hz, we can notice that ϵ_{d} is almost negligible. However, for high and very high mobility vehicular scenarios, where $f_{\mathrm{d}} > 500$ Hz, Doppler interference starts recording a considerable impact on the overall performance.

We note that the proposed estimators adhere to the IEEE

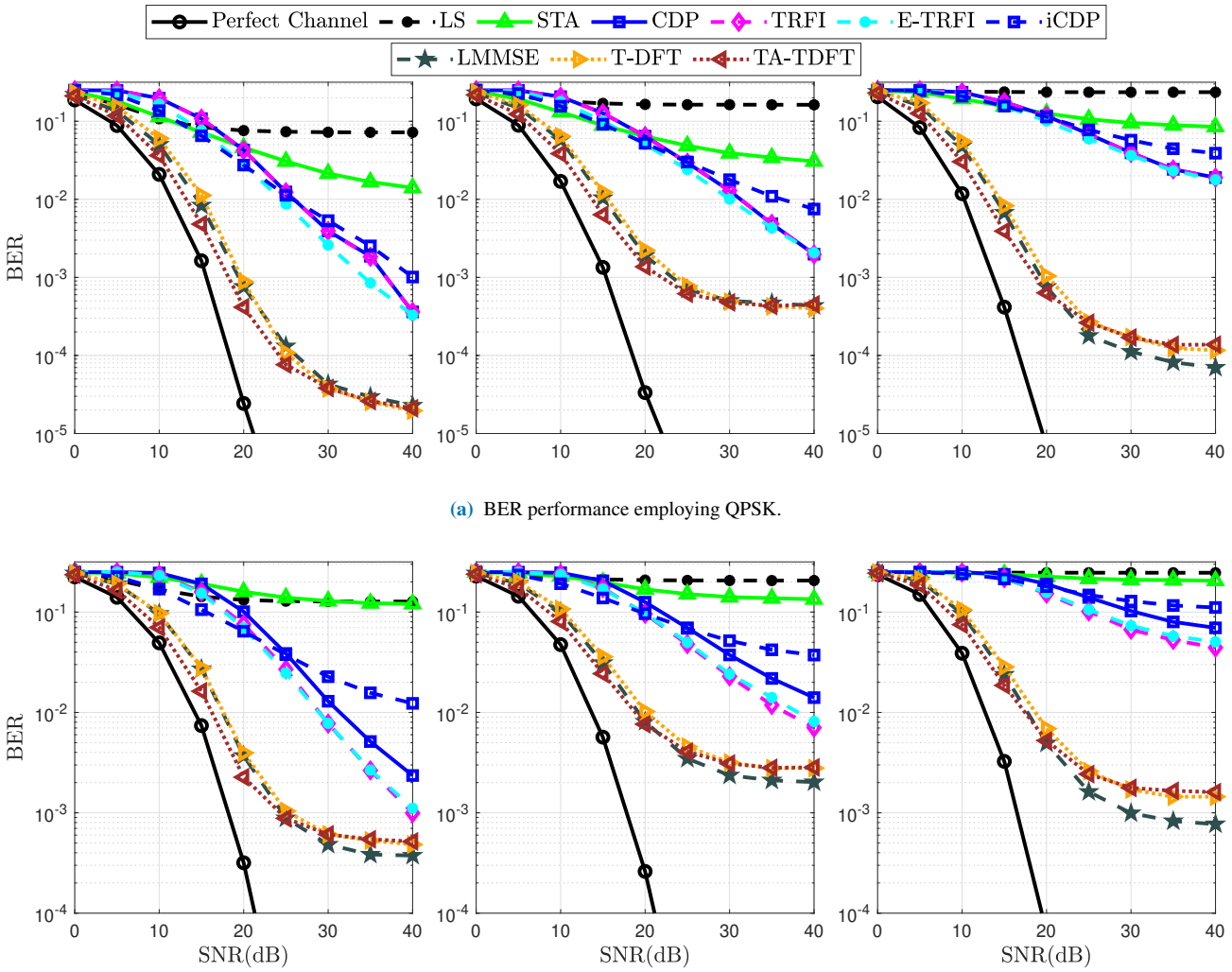

(a) BER performance employing QPSK.

(b) BER performance employing 16QAM.

FIGURE 8: BER performance employing three scenarios: (*i*) first column - low mobility ($v = 45$ Kmph, $f_d = 250$ Hz) (*ii*) second column - high mobility ($v = 100$ Kmph, $f_d = 500$ Hz) (*iii*) third column - very high mobility ($v = 200$ Kmph, $f_d = 1000$ Hz).

802.11p standard structure, and the transmission data rates in all modulation orders are preserved. Moreover, employing T-DFT and TA-TDFT estimators outperform conventional estimators with a considerable performance improvement and a significant decrease in the overall computational complexity as shown in Section VI.

B. BER EVALUATION

Figure 8 shows the BER performance of the studied estimators employing QPSK and 16QAM modulations in low mobility, high mobility, and very high mobility scenarios. For QPSK modulation order, the STA estimator outperforms other conventional estimators in low SNR regions due to the frequency and time averaging operations used in STA (17), (18). Whereas in high SNR regions, conventional estimators express a significant improvement over the STA estimator, where CDP and TRFI record similar performance. This is due to the fact that when the SNR is low, the impact of noise and interference is high and powerful enough to shift the equalized received OFDM symbol $\boldsymbol{y}_{\text{eq}_i}[k]$ to wrong regions and as a result, its demapping $\boldsymbol{d}_i[k]$ is shifted to incorrect constellation points. The STA estimator averaging operations are able to alleviate the impact of the noise. However, as the SNR increases, the aforementioned influence is reduced, and thus, the superiority of the conventional estimators emerges over STA. It is worth mentioning that the STA estimator frequency-domain averaging window β, and the time-domain averaging coefficient α are fixed to 2 as discussed in [7]. But, fixing these parameters instead of updating them according to the channel variation makes the smoothing in the time and frequency domains not effective under vehicular environment. Thus, the gradually accumulated demapping error of $\boldsymbol{d}_i[k]$ cannot be well mitigated using fixed β and α. Hence the emergence of the error floor for STA in high SNR region. On the other hand, the iCDP estimator improves the STA estimator performance by considering both

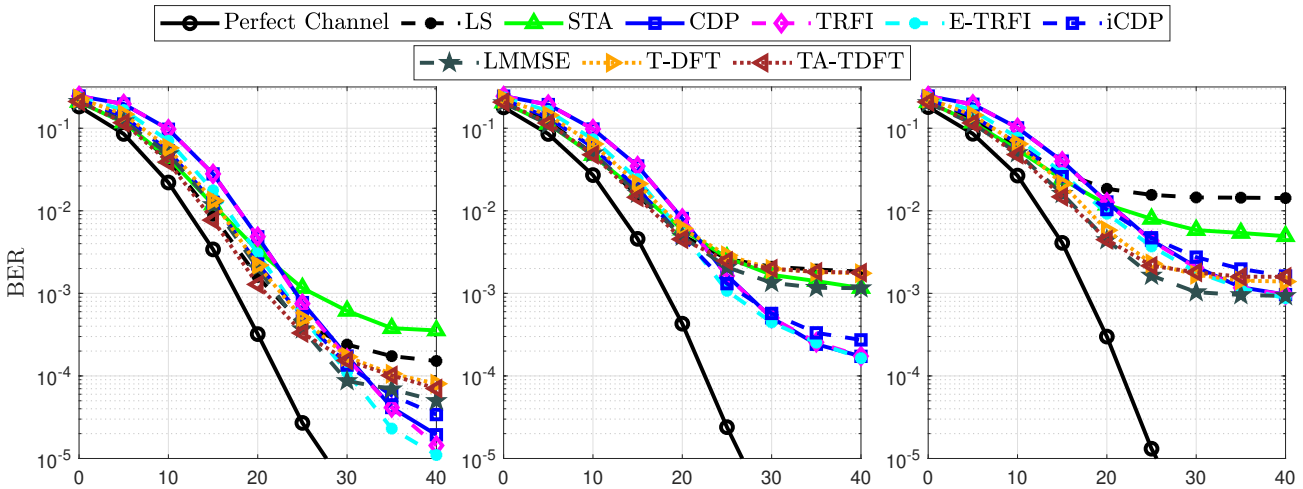

(a) BER performance with $I = 10$.

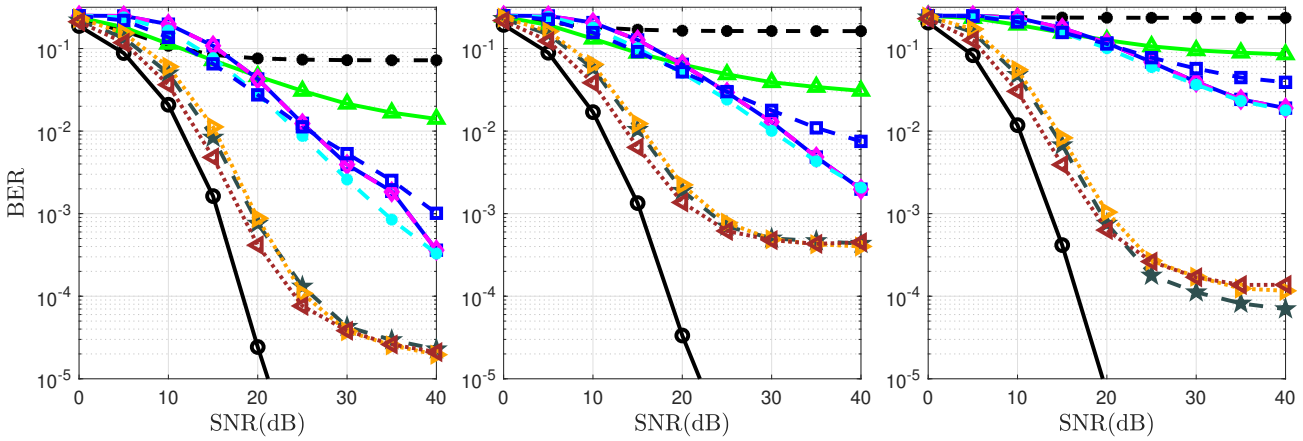

(b) BER performance with $I = 100$.

FIGURE 9: BER performance employing three scenarios: (*i*) first column - low mobility ($v = 45$ Kmph, $f_d = 250$ Hz) (*ii*) second column - high mobility ($v = 100$ Kmph, $f_d = 500$ Hz) (*iii*) third column - very high mobility ($v = 200$ Kmph, $f_d = 1000$ Hz).

STA and DPA estimations in updating the final iCDP channel estimates. We can notice that employing the iCDP estimator alleviates the STA estimator error floor in high SNR regions while recording almost similar performance as STA in low SNR regions.

When 16QAM modulation is employed, STA performance is severely degraded in the whole SNR region due to the huge DPA demapping error that increases as the modulation order increases. Moreover, we can notice the impact of employing the cubic interpolation in TRFI, where it outperforms CDP by around 2dB gain. On the other hand, E-TRFI is not able to improve the TRFI estimator performance due to fixing the E-TRFI reliability test threshold to 0.5 as provided in [11].

We note that conventional estimators performance is limited due to their dependency on the DPA estimation and due to using fixed valued parameters. These two reasons are mainly responsible for the conventional estimators performance degradation in time-variant channel estimation as shown in Figure 6a and Figure 6b. In contrast, we can notice the performance superiority of the LMMSE over the conventional DPA-based estimators due to employing the channel and noise statistics in the channel estimation process. However, the robustness of the LMMSE estimator is limited in the online evaluation, when there is a significant mismatch between the estimated and real channel statistics. In contrast, the proposed T-DFT and TA-TDFT estimators do not depend on the DPA estimation and estimated channel statistics, thus the demapping error is totally eliminated, resulting in improving the overall estimation performance. Moreover, they record a robustness superiority over the LMMSE estimator as shown in Section V-C.

The impact of employing different frame lengths is illustrated in Figure 9. We can notice that the conventional DPA-based estimators perform better when shorter frame length is employed since the impact of the enlarged demapping error and channel variation is negligible compared to the case

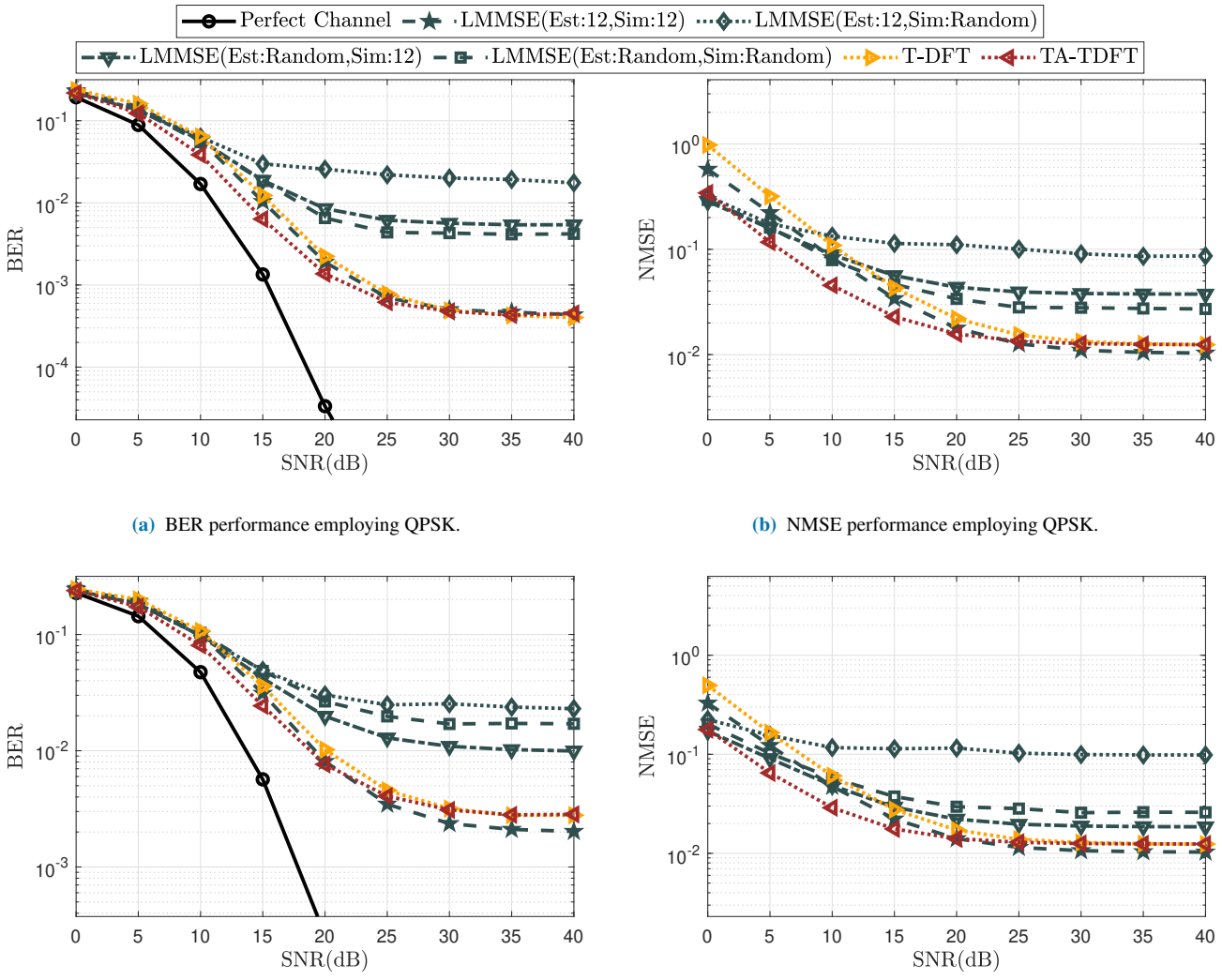

(a) BER performance employing QPSK.

(b) NMSE performance employing QPSK.

(c) BER performance employing 16QAM.

(d) NMSE performance employing 16QAM.

FIGURE 10: Robustness analysis of the proposed DFT-based estimators versus the LMMSE estimator in high mobility channel model ($f_d = 500$ Hz).

where long frames are employed. Moreover, the impact of employing temporal averaging on top of the T-DFT estimator to improve the overall performance can be observed, where the TA-TDFT estimator outperforms the T-DFT estimator by up to 3 dB gain in terms of SNR for a BER = 10^{-3} for a long frame ($I = 100$), whereas the impact in a short frame ($I = 10$) is less significant.

It is worth mentioning that the impact of mobility and frame length can be observed in the significant decrease of BER when using long frames. This is due to the use of a long codeword and the harvested time diversity gain. The time diversity gain increases with the increase of the Doppler spread, as can be seen by comparing the case of high mobility ($f_d = 500$) and very high mobility ($f_d = 1000$). Nevertheless, as the channel estimation error increases with the increase of Doppler frequency, the net gain from the time diversity and channel estimation loss depends also on the frame length. For instance, assuming a perfect channel, there is a small net gain with ($I = 100$), when the Doppler shift increases from $f_d = 250$ in low mobility to $f_d = 500$ in high mobility, but it turns to a small loss for short frames ($I = 10$). The perfect estimation is only influenced by Doppler interference. With the induced estimation error, this impact becomes remarkable. The performance of the presented estimators is significantly degraded by the mobility increase, however, it is improved in high mobility for long frames. This observation is also valid for high modulation orders such as 16QAM, as shown in Figure 8.

C. ROBUSTNESS ANALYSIS

This section compares the robustness and generalization ability of the proposed T-DFT and TA-TDFT estimators with the LMMSE estimator. As discussed in III-D, the LMMSE estimator depends mainly on the pre-estimated $\boldsymbol{W}_{\text{LMMSE}}$ matrix

that is calculated offline. This offline pre-estimation affects the robustness and generalization ability of the LMMSE estimator when the channel changes in the online evaluation. To further illustrate this idea, we simulate the LMMSE estimator in four different cases, such that:

- Case 1 (Est: 12, Sim: 12): $\boldsymbol{W}_{\text{LMMSE}}$ is pre-estimated using the 12 taps channel model and we consider that the number of taps is fixed also in the online testing.
- Case 2 (Est: 12, Sim: Random): $\boldsymbol{W}_{\text{LMMSE}}$ is pre-estimated using the 12 taps channel model. However, the number of channel taps changes randomly in the online testing. We note that the "Random" term means that the simulation is carried using a random number of paths, wherein each iteration, a random number of paths between 1 and 11 is eliminated from the channel power delay profile. Therefore, we obtain a generalized channel model where the number of taps varies.
- Case 3 (Est: Random, Sim: 12): $\boldsymbol{W}_{\text{LMMSE}}$ is pre-estimated where the number of channel taps varies randomly, while the channel taps are fixed to 12 in the online testing.
- Case 4 (Est: Random, Sim: Random): Random number of channel taps are used in both offline estimation of $\boldsymbol{W}_{\text{LMMSE}}$ and in the online testing.

Figure 10 depicts the simulation results of these four cases in high mobility scenario employing both QPSK and 16QAM modulation orders. We can observe that the LMMSE performance is severely degraded when the channel changes in the online evaluation, whereas, the proposed TDFT and TA-TDFT estimators reveal good robustness since they are implemented without any dependency on the channel model statistics. Therefore, the proposed TDFT and TA-TDFT estimators are more robust than the LMMSE estimator.

VI. COMPLEXITY ANALYSIS

In this section, a detailed computational complexity and execution time analysis of the conventional and the proposed estimators are provided. The computational complexity analysis is performed according to the number of real-valued multiplication/division and summation/subtraction mathematical operations required to estimate the channel for one received OFDM symbol. Since we are working with complex-valued data, each complex-valued division requires 6 real-valued multiplications, 2 real-valued divisions, 2 real-valued summations, and 1 real-valued subtraction. Moreover, each complex-valued multiplication is equivalent to 4 real-valued multiplications, and 3 real-valued summations.

The least complex estimator is the basic LS estimator (14) where the received preamble symbols are added to each others, resulting in $2K_{\text{on}}$ summations. After that, the summation result is divided by the predefined preamble, thus $2K_{\text{on}}$ divisions are also required. Therefore, the total number of divisions and summations needed by the basic LS estimator is $2K_{\text{on}}$ and $2K_{\text{on}}$ respectively.

The DPA estimation requires two equalization steps (15), and (16). Each equalization step consists of K_{on} complex-valued division, therefore the overall computational complexity of DPA is $16K_{\text{on}}$ multiplications/divisions and $6K_{\text{on}}$ summations/subtractions.

The STA estimator applies frequency and time-domain averaging on top of DPA. The frequency-domain averaging (17) coefficient is fixed ($\beta = 2$). Therefore, each subcarrier requires 5 complex-valued summations multiplied by a real-valued weight, which are equivalent to 10 real-valued summations and 2 real-valued multiplications. But the frequency averaging in the STA estimator is applied on K_d since the subcarriers in the boundaries are excluded from the averaging operation. As a result, the STA frequency-domain averaging step requires $10K_d$ real-valued summations and $2K_d$ real-valued multiplications. Moreover, the STA time-domain averaging step (18) requires $4K_{\text{on}}$ real-valued divisions, and $2K_{\text{on}}$ real-valued summations. Therefore, the computational complexity of STA is $4K_{\text{on}} + 2K_d$ real-valued multiplications/divisions, and $2K_{\text{on}} + 10K_d$ real-valued summations/subtractions, and the accumulated overall computational complexity of STA estimator is $22K_{\text{on}} + 2K_{\text{d}}$ multiplications/divisions and $10K_{\text{on}} + 10K_{\text{d}}$ summations/subtractions.

For the E-TRFI estimator, it starts with the E-LS estimation step (19) that requires $4K_{\text{on}}K$ real-valued multiplications and $5K_{\text{on}}K - 2K$ real-valued summations. Then equalization is employed only on K_d subcarriers where $8K_d$ multiplications/divisions and $3K_d$ summations/subtractions are required. The Euclidean distance reliability test employs $K_d + 2MK_d$ real-valued divisions and $4MK_d$ subtractions. After that, frequency-domain cubic interpolation is performed. Our simulations show that for each OFDM symbol, $K_{\text{URS}} = 16$ subcarriers needed to be interpolated. The frequency-domain cubic interpolation requires $26K_{\text{URS}}$ multiplications/divisions and $30K_{\text{URS}}$ summations/subtractions. Finally, the E-TRFI employs the noise attenuation step that requires $4K^2$ real-valued multiplications and $5K^2 - 2K$ real-valued summations. Hence, the E-TRFI estimator's overall computational complexity is $4K^2 + 4KK_{\text{on}} + 9K_{\text{d}} + 26K_{\text{URS}}$ multiplications/divisions and $5K^2 + 5KK_{\text{on}} + 3K_{\text{d}} + 2MK_{\text{d}} + 30K_{\text{URS}} - 4K$ real-valued summations/subtractions.

The LMMSE estimator manipulates first the LS estimation at the pilot subcarriers within the received OFDM symbol which requires $2K_{\text{p}}$ real-valued divisions. After that, the matrix inversion in (27) requires K_p^3 complex-valued multiplication. Accordingly, the overall computational complexity of the conventional LMMSE estimator is $4K_{\text{p}}^3 + 4K_{\text{p}}K_{\text{d}} + 2K_{\text{p}}$ real-valued multiplications/divisions and $3K_{\text{p}}^3 + 2K_{\text{p}}^2 + 5K_{\text{p}}K_{\text{d}} - 2K_{\text{d}}$ real-valued summations.

Compared to the conventional estimators, the T-DFT estimator does not require the DPA as a pre-estimation step. It only requires the LS estimated channel at pilot subcarriers $\tilde{\boldsymbol{h}}_{i,p}$ that requires $2K_{\text{p}}$ divisions. It is worth mentioning that $\boldsymbol{W}_{\text{MDFT}}$ is computed offline, thus the computational complexity of the T-DFT estimator lies in multiplying $\boldsymbol{W}_{\text{MDFT}}$ with $\hat{\tilde{\boldsymbol{h}}}_{i,p}$ which requires $K_pK_d - K_d$ complex-

TABLE 4: Computational complexity analysis of the SoA SBS channel estimators.

Est.	Pre-Est.	Mul. / Div.	Sum. / Sub.
LS	-	$2K_{\text{on}}$	$2K_{\text{on}}$
DPA	LS	$18K_{\text{on}}$	$8K_{\text{on}}$
STA	DPA	$22K_{\text{on}} + 2K_{\text{d}}$	$10K_{\text{on}} + 10K_{\text{d}}$
CDP	DPA	$34K_{\text{d}}$	$14K_{\text{d}}$
TRFI	DPA	$34K_{\text{on}} + 26K_{\text{URS}}$	$14K_{\text{on}} + 30K_{\text{URS}}$
iCDP	DPA , STA	$58K_{\text{on}} + 2K_{\text{d}}$	$26K_{\text{on}} + 10K_{\text{d}}$
E-TRFI	DPA	$4K^2 + 4K_{\text{on}}K + 2MK_d + 26K_{\text{URS}}$	$5K^2 + 5K_{\text{on}}K + 3K_d + 4MK_d + 30K_{\text{URS}} - 4K$
LMMSE	$\hat{\tilde{\boldsymbol{h}}}_{p_i}, \boldsymbol{R}_{\tilde{\boldsymbol{h}}_i,\tilde{\boldsymbol{h}}_{p_i}}, \boldsymbol{R}_{\tilde{\boldsymbol{h}}_{p_i},\tilde{\boldsymbol{h}}_{p_i}}$	$4K_{\text{p}}^3 + 4K_{\text{p}}K_{\text{d}} + 2K_{\text{p}}$	$3K_{\text{p}}^3 + 2K_{\text{p}}^2 + 5K_{\text{p}}K_{\text{d}} - 2K_{\text{d}}$

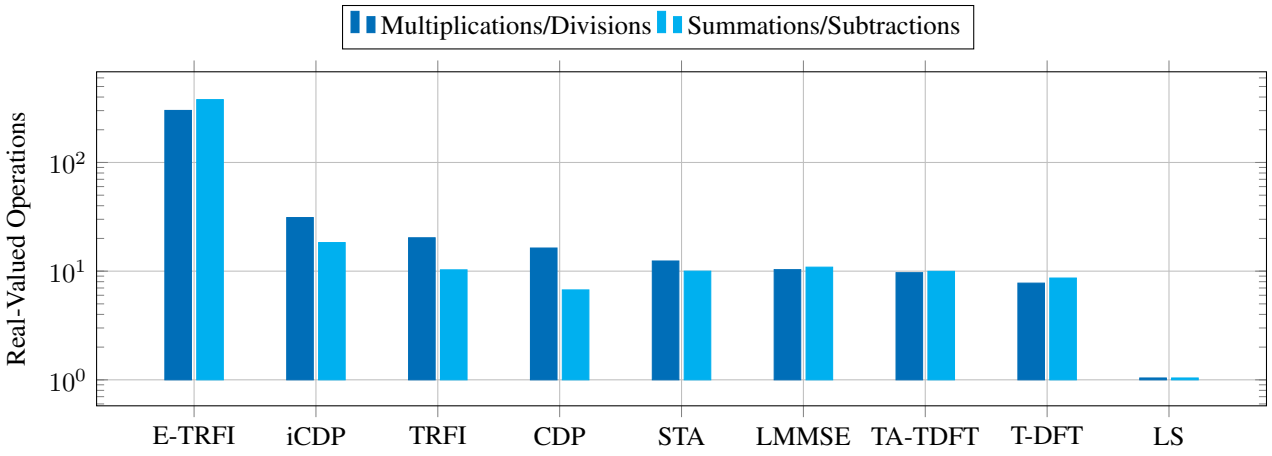

FIGURE 11: Detailed computational complexity of the SoA SBS channel estimators in terms of real-valued operations.

valued summations, and K_pK_d complex-valued multiplications, that are equivalent to $5K_{\text{p}}K_d - 2K_d$ real-valued summations, and $4K_pK_d$ real-valued multiplications. Therefore the overall computational complexity of the T-DFT estimator is $2K_p + 4K_pK_d$ real-valued multiplications/divisions, and $5K_pK_d - 2K_d$ real-valued summations. On the other hand, the TA-TDFT estimator applies simple time averaging on top of the T-DFT estimator that requires additional $4K_d$ real-valued multiplications, and $2K_d$ real-valued summations. As a result, TA-TDFT estimator requires $2K_p + 4K_d + 4K_pK_d$ real-valued multiplications/divisions, and $5K_pK_d$ real-valued summations.

It is worth mentioning that the proposed estimators achieve better BER and NMSE performance than the studied conventional estimators, while reducing the computational complexity, by which TA-TDFT and T-DFT record 22.64% and 7.35% computational complexity decrease than the conventional LMMSE estimator, respectively. Moreover, the TA-TDFT estimator has a complexity higher than the T-DFT estimator by 17.56% as illustrated in 11.

Table 4 shows a detailed summary of the computational complexities for studied estimators. We note that the detailed calculation of TRFI, CDP, iCDP estimators is presented in [9], [24].

Figure 11 show a bar graph for the required multiplications/divisions, and summations/subtractions by the studied estimators. It can be noticed that employing both T-DFT and TA-TDFT instead of the studied conventional estimators leads to a significant decrease in the overall computational complexity compared to the conventional DPA-based and LMMSE estimators, while recording a considerable gain in BER and NMSE performance.

On the other hand, the proposed estimators record less execution time than the conventional estimators as can be observed in Table 5. We note that the simulations are performed using a 64-bit operating system with an Intel Core i7-8850H CPU processor (clock speed: 2.60 GHz).

VII. CONCLUSIONS AND PERSPECTIVES

In this paper, we have focused on overcoming the limitations of vehicular SoA conventional estimators represented by their dependency on the DPA estimation, where the demapping error and the noise are enlarged during the estimation process. To overcome these limitations, we have proposed low-complexity and robust channel estimators for vehicular communications, namely T-DFT and TA-TDFT. Unlike classical estimators, the proposed estimators are based on the truncated DFT-based interpolation and do not require the DPA estimation as an initial estimation step. Therefore, the enlarged DPA demapping error and the noise enhancement that results from the basic LS estimator are totally eliminated in the proposed estimators. In addition to that, the proposed

TABLE 5: CPU execution time analysis of the studied estimators.

Est.	E-TRFI	TRFI	iCDP	CDP	STA	LMMSE	TA-TDFT	T-DFT
Execution time	$1.23\ ms$	$0.93\ ms$	$0.76\ ms$	$0.68\ ms$	$0.24\ ms$	$1.24\ \mu s$	$0.46\ \mu s$	$0.38\ \mu s$

estimators do not depend on the pre-estimated channel statistics as it is the case for LMMSE estimator, thus, they are insensitive against channel model changes. Therefore, they are more suitable to be employed in practical systems. Simulation and analytical results have shown the performance superiority of the proposed T-DFT and TA-TDFT estimators over conventional estimators in low and high mobility vehicular scenarios with a significant computational complexity and execution time decrease.

As future work, we will extend our analysis to the IEEE 802.11bd standard as well as cellular-based vehicular communications settings. A detailed investigation in terms of performance, complexity and latency will be conducted. However, inspired by the work proposed in [25], [26], it is expected that the new features of the upcoming IEEE 802.11bd standard will significantly improve the channel estimation accuracy compared to the IEEE 802.11p standard. Moreover, it is worthwhile to see if the performance gain of employing the IEEE 802.11bd standard will be able to alleviate efficiently the DPA demapping error of the SoA estimators, or it will be the same case as the IEEE 802.11p standard.

REFERENCES

[1] P. Alexander, D. Haley, and A. Grant, "Cooperative Intelligent Transport Systems: 5.9-GHz Field Trials," Proceedings of the IEEE, vol. 99, no. 7, pp. 1213–1235, 2011.
[2] J. J. Rolison, S. Regev, S. Moutari, and A. Feeney, "What are the Factors that Contribute to Road Accidents? An Assessment of Law Enforcement Views, Ordinary Drivers' Opinions, and Road Accident Records," Accident Analysis & Prevention, vol. 115, pp. 11–24, 2018.
[3] F. Qu, F. Wang, and L. Yang, "Intelligent Transportation Spaces: Vehicles, Traffic, Communications, and Beyond," IEEE Communications Magazine, vol. 48, no. 11, pp. 136–142, 2010.
[4] Y. Yang, D. Fei, and S. Dang, "Inter-vehicle Cooperation Channel Estimation for IEEE 802.11p V2I Communications," Journal of Communications and Networks, vol. 19, no. 3, pp. 227–238, 2017.
[5] Y. Yang, S. Dang, Y. He, and M. Guizani, "Markov Decision-Based Pilot Optimization for 5G V2X Vehicular Communications," IEEE Internet of Things Journal, vol. 6, no. 1, pp. 1090–1103, 2019.
[6] A. Abdelgader and L. Wu, "The Physical Layer of the IEEE 802.11 p WAVE Communication Standard: The Specifications and Challenges," Lecture Notes in Engineering and Computer Science, vol. 2, Oct, 2014.
[7] J. A. Fernandez, K. Borries, L. Cheng, B. V. K. Vijaya Kumar, D. D. Stancil, and F. Bai, "Performance of the 802.11p Physical Layer in Vehicle-to-Vehicle Environments," IEEE Transactions on Vehicular Technology, vol. 61, no. 1, pp. 3–14, 2012.
[8] Z. Zhao, X. Cheng, M. Wen, B. Jiao, and C. Wang, "Channel Estimation Schemes for IEEE 802.11p Standard," IEEE Intelligent Transportation Systems Magazine, vol. 5, no. 4, pp. 38–49, 2013.
[9] C. G. Wang, Hussain, "An Improved Channel Estimation Technique for IEEE 802.11p Standard in Vehicular Communications," Sensors (Basel, Switzerland), vol. 19, no. 1, 2018.
[10] Yoon-Kyeong Kim, Jang-Mi Oh, Yoo-Ho Shin, and Cheol Mun, "Time and Frequency Domain Channel Estimation Scheme for IEEE 802.11p," in 17th International IEEE Conference on Intelligent Transportation Systems (ITSC), 2014, pp. 1085–1090.
[11] S. Han, J. Park, and C. Song, "Virtual Subcarrier Aided Channel Estimation Schemes for Tracking Rapid Time Variant Channels in IEEE 802.11p Systems," in 2020 IEEE 91st Vehicular Technology Conference (VTC2020-Spring), 2020, pp. 1–5.
[12] Y. Choi, J. H. Bae, and J. Lee, "Low-Complexity 2D LMMSE Channel Estimation for OFDM Systems," in 2015 IEEE 82nd Vehicular Technology Conference (VTC2015-Fall), 2015, pp. 1–5.
[13] X. Weidong, G. Javier, N. Zhisheng, A. Onur, and E. Eylem, "Wireless Access in Vehicular Environments," EURASIP Journal on Wireless Communications and Networking, vol. 1, pp. 1687–1499, 2009.
[14] G. Matz and F. Hlawatsch, "Chapter 1 - Fundamentals of Time-Varying Communication Channels," in Wireless Communications Over Rapidly Time-Varying Channels, 2011, pp. 1–63.
[15] N. D. Ricklin, "Time Varying Channels : Characterization, Estimation, and Detection," Ph.D. dissertation, University of California, San Diego, 2010.
[16] C. F. Mecklenbrauker, A. F. Molisch, J. Karedal, F. Tufvesson, A. Paier, L. Bernado, T. Zemen, O. Klemp, and N. Czink, "Vehicular Channel Characterization and Its Implications for Wireless System Design and Performance," Proceedings of the IEEE, vol. 99, no. 7, pp. 1189–1212, 2011.
[17] C. Wang, X. Cheng, and D. I. Laurenson, "Vehicle-to-Vehicle Channel Modeling and Measurements: Recent Advances and Future Challenges," IEEE Communications Magazine, vol. 47, no. 11, pp. 96–103, 2009.
[18] J. Karedal, F. Tufvesson, N. Czink, A. Paier, C. Dumard, T. Zemen, C. F. Mecklenbrauker, and A. F. Molisch, "A Geometry-based Stochastic MIMO Model for Vehicle-to-Vehicle Communications," IEEE Transactions on Wireless Communications, vol. 8, no. 7, pp. 3646–3657, 2009.
[19] W. Viriyasitavat, M. Boban, H. Tsai, and A. Vasilakos, "Vehicular Communications: Survey and Challenges of Channel and Propagation Models," IEEE Vehicular Technology Magazine, vol. 10, no. 2, pp. 55–66, 2015.
[20] G. Acosta-Marum and M. A. Ingram, "Six Time and Frequency Selective Empirical Channel Models for Vehicular Wireless LANs," IEEE Vehicular Technology Magazine, vol. 2, no. 4, pp. 4–11, 2007.
[21] G. Acosta-Marum, "Measurement, Modeling, and OFDM Synchronization for the Wideband Mobile-to-Mobile Channel," Ph.D. dissertation, Georgia Inst. Technol., Atlanta, GA, 2007.
[22] M. Marsden, "Cubic Spline Interpolation of Continuous Functions," Journal of Approximation Theory, vol. 10, no. 2, pp. 103–111, 1974.
[23] S. Biyyam and A. Bhuma, "Optimal Channel Estimation Using DFT-Based Interpolation with Comb-Type Pilots for OFDM Systems," in Innovations in Electronics and Communication Engineering, 2018, pp. 473–484.
[24] A. K. Gizzini, M. Chafii, A. Nimr, and G. Fettweis, "Deep Learning Based Channel Estimation Schemes for IEEE 802.11p Standard," IEEE Access, vol. 8, pp. 113 751–113 765, 2020.
[25] A. Karim Gizzini, M. Chafii, A. Nimr, R. M. Shubair, and G. Fettweis, "CNN Aided Weighted Interpolation for Channel Estimation in Vehicular Communications," IEEE Transactions on Vehicular Technology, vol. 70, no. 12, pp. 12 796–12 811, 2021.
[26] S. Ehsanfar, K. Moessner, A. Karim Gizzini, and M. Chafii, "Performance Comparison of IEEE 802.11p, 802.11bd-draft and a Unique Word-based PHY in Doubly-Dispersive Channels," in 2022 IEEE Wireless Communications and Networking Conference (WCNC), 2022.

ABDUL KARIM GIZZINI Received his Ph.D. degree in telecommunications engineering in 2021 from Cergy Paris CY University in France. His Master's and bachelor's degrees in computer and communication engineering in 2017 and 2015, both from IUL university in Lebanon. His master thesis was conducted in collaboration with the Lebanese National Council for Scientific Research (CNRS). During 2020 he has been a visiting researcher at Vodafone Chair Mobile Communications Systems, Technical University of Dresden - Germany. Moreover, he has an active research collaboration with Technical University of Chemnitz - Germany, National Institute of Telecommunications (Inatel) - Brazil, New York University (NYU) - Abu Dhabi, CNRS - Lebanon. His research interests include vehicular communications, channel estimation in doubly dispersive channels, and artificial intelligence for wireless communications and image processing. He is currently a post-doctoral researcher at ETIS laboratory (UMR8051) which is a joint research unit between ENSEA, CY University, and CNRS in France.

MARWA CHAFII received her Ph.D. degree in electrical engineering in 2016, and her Master's degree in the field of advanced wireless communication systems (SAR) in 2013, both from CentraleSupélec, France. Between 2014 and 2016, she has been a visiting researcher at Poznan University of Technology (Poland), University of York (UK), Yokohama National University (Japan), and University of Oxford (UK). She joined the Technical University of Dresden, Germany, in 2018 as a research group leader, and ENSEA, France, in 2019 as an associate professor where she held a Chair of Excellence on Artificial Intelligence from CY Initiative. Since September 2021, she is an associate professor at New York University (NYU) Abu Dhabi, and NYU WIRELESS, NYU Tandon School of Engineering. Her research interests include advanced waveform design, machine learning for wireless communications, and indoor localization. She received the prize of the best Ph.D. in France in the fields of Signal, Image & Vision, and she has been nominated in the top 10 Rising Stars in Computer Networking and Communications by N2Women in 2020. She served as Associate Editor at IEEE Communications Letters 2019-2021, where she received the Best Editor Award in 2020. Between 2018 and 2021, she was research lead at the Women in AI organization. She is currently vice-chair of the IEEE ComSoc ETI on Machine Learning for Communications and leading the Education working group of the ETI on Integrated Sensing and Communications.